Physical Conditions in Quiescent Dark Cloud Cores Determined From Multitransition Observations of CCS

Debra Wolkovitch[1]

National Astronomy and Ionosphere Center, Department of Astronomy, Cornell University, Ithaca NY 14853

William D. Langer

Jet Propulsion Laboratory, California Institute of Technology, Pasadena CA 91109

Paul F. Goldsmith[2]

National Astronomy and Ionosphere Center, Department of Astronomy, Cornell University, Ithaca NY 14850

and

Mark Heyer

Five College Radio Astronomy Observatory, Department of Physics and Astronomy, University of Massachusetts, Amherst MA 01003

ABSTRACT

We have studied three transitions of the CCS molecule to determine physical conditions in L1498 and TMC1-D. two narrow-line dense cores in the Taurus region. We observed the $NJ = 1_2 - 0_1, 3_4 -- 2_3$, and $7_8 - 6_7$ transitions at 22.3, 45.4. and 93.9 GHz, respectively, at 50" angular resolution. The intensities 01' the emission lines have been analyzed using statistical equilibrium calculations and collision rates calculated for the CCS-H_2 system. These were obtained from the Molscat scattering code together with inclusion of spin dependence in Hund's case (b) model. We find that the kinetic temperature in both sources is extremely low, between 7 and 10 K. The L1498 emission appears to originate in a single velocity component with mean hydrogen density 3 to 14 x 10^4 cm^3. We analyzed three velocity components in TMC 1-D separately, and find that the low-velocity component has a mean H_2 density of 6 X $10^3 cm^{-3}$, while the two higher-velocity components are denser by approximately a factor of three. The L1498 core is close to virial equilibrium in that the magnitude of its gravitational energy is close to that of its kinetic energy. However, the cores corresponding; to the three velocity components in TMC-1D are unbound by factors of two to seven.

---

[1] Present address: IGPP-UCLA, Room 5345 Slichter Hall, Los Angeles, CA 90095-1567

[2] Send reprint requests to pfg@astrosun.tn.cornell.edu

Subject headings: ISM: individual (Taurus, L1498)- ISM: molecules (CCS) - p h y s i c a l conditions

We dedicate this paper to the memory of Sheldon Green, who passed away in December 1995. Sheldon was an outstanding chemist who made many significant contributions to molecular astrophysics.

1. Introduction

Dark clouds are the less massive and colder subset of molecular clouds, with typical masses 10^2-$10^3 M_\odot$ and kinetic temperatures 8-15 K. Specifically, low mass $(M \sim 1 M_\odot)$ star formation is thought to occur in sub-condensations of dark molecular clouds known as *dense cores*. The association between these cores and stars is significantly larger than would occur through random scattering of stars in dark clouds. For example, Beichman et al. (1986) used the iii,-\S survey to search for newly formed stars in nearby dense cores, and found IRAS sources in 47 01' 95 dense cores surveyed.

Myers, Linke & Benson (1983) conducted the first large radio survey of dense cores. They identified nearly 100 cores as small $(\leq .5')$ spots of visual extinction on Palomar plates. They then confirmed the classification of these regions as dense cores by observing corresponding enhanced emission in the $J = 1 - . 0$ transition of ^{13}CO and C^{18}O. Mapping studies of cores reveal that they tend to be centrally condensed and that there may be a clumpy substructure GO the gas they contain as well (Snell, Langer & Frerking 1982, Langer et al. 1995). Myers & Benson (1983) conducted a survey which indicates that most dense cores appear to be close to virial equilibrium or in the early phase of collapse. However, the uncertainty in their derived core masses and sizes clid not allow them to determine definitively if cores are gravitationally bound entities or simply transient aggregations of gas. A similar question arises for clumps which have been detected within the cores.

Most cores are not spherical, but have aspect ratios of $\sim 1:2$, and may have a complex internal structure as well. About half of the cores in the Benson & Myers (1989) study exhibited non-gaussian spectral line-shapes, possibly indicating the presence of internal structure. naps of cores in various molecular species demonstrate that different molecular tracers may reveal very different morphologies within the same core (Suzuki et al. 1984, Myers et al. 1991, Swa de 1989). These differences may result from variations in temperature, density, chemical abundances within a core, further complicating the picture 01' these objects.

An interesting feature of many of the cores in the NH$_3$ survey of Benson & Myers (1989) is their remarkably narrow linewidths, which range from 0.20 to 1.38 $km\ s^{-1}$. For comparison, the thermal linewidth of NH$_3$ at 10 K is 0.17 $km\ s^{-1}$ Cores which are associated with IRAS sources have considerably larger linewidths than starless cores. Thus, either the stars themselves produce large-scale turbulent motions within the cores through mechanisms such as stellar outflows, or the processes leading up to star formation cause turbulence. Many of the starless cores in the NH$_3$ survey have a linewidth barely larger than that due to thermal Doppler broadening. Such narrow lines indicate a low level of turbulent motions in the core. The linewidth of emission lines in a, core is a result of both thermal Doppler broadening and non-thermal motions of the gas which add in quadrature to give the total observed linewidth, i.e.

$$(\Delta V_{tot})^2 = (\Delta V_t)^2 + (\Delta V_{nt})^2. \tag{1}$$

The thermal linewidth has the form $\Delta V_t = 2(2ln(2)kT/m)^{0.5}$ where k is Boltzmann's constant,

T is the kinetic temperature of the gas, and m is the mass of the observed molecule. The non-thermal portion of the linewidth may arise from such phenomena as rotation, gravitational collapse, turbulence, or other large scale motions within the core. Fuller & Myers (1992) showed that turbulent motions tend to increase with increasing core size.

Because non-thermal velocity dispersions as small as 0.04 $km\,s^{-1}$ have been observed in dense cores (Fuller & Myers, 1993; Langer et al. 1995), it is advantageous to employ a molecule with a comparable or smaller thermal dispersion to study dense cores. For a kinetic temperature of 10K, an ideal molecular tracer would have a mass > 50 amu. Long carbon chain molecules, including the cyanopolyyenes ($HC_{2n+1}N$, n = 1, 2, 3, 4, j), C_nH (n = 1. 2,3. 4, 5, 6) and C_nS (n=1.2.3) thus make good tracers of dense regions. Additionally, long chain molecules have large moments of inertia, producing closely spaced rotational energy levels, which yield many observable transitions. The abundances of different kinds of carbon chain molecules in a core are often correlated. Suzuki et al. (1992) postulate that carbon chain molecules are abundant in early evolutionary periods of cores, and become less common at later times as the carbon tends to become bound up into CO. In their survey of CCS in dense cores, they noted that CCS was significantly more likely to be found in cores without stars than in cores with stars. They also found this molecule to be widespread, detecting CCS in 68% of cores observed in the Taurus region. Thus, CCS should be a good molecule with which to determine conditions in pre-protostellar cores.

To use CCS as a tracer we must be able to predict its line emission under a variety of physical conditions. CCS has no hyperfine structure. which simplifies interpretation of its spectra. particularly in regions with narrow spectral lines. However, CCS has electronic angular momentum due to spin, complicating determination of its energy levels and collisional cross sections. In this paper we consider in some detail the excitation of CCS and use our calculated collision rates to analyze observations of three CCS transitions. With this information we determine physical conditions in L1498 and TMC1-D, two narrow-line dense cores in the Taurus molecular cloud region.

2. CCS Excitation

In order to determine physical conditions, we require a statistical equilibrium Calculation of level populations and line intensities. We utilized the large velocity gradient (LVG) model (Goldreich & Kwan 1974). We emphasize that for modest optical depths, the form of the velocity gradient, or in fact the choice of radiative transfer model, is not critical, and the LVG model is adopted here essentially as a convenience rather than due to any assumption that these cores are, in fact, in symmetrical radial motion. This approach is justified by the conclusion (see below) that the CCS optical depths, although not always small, do not significantly exceed unity.

For the CCS lines we have observed, spontaneous decay rates range from 4 X $10^{-7}s^{-1}$ to 4 'x 1 05 s^{-1}, while collision rate coefficients are 2 to 9 x $10^{-11}cm^3\,s^{-1}$, yielding critical

densities of approximately 3 x $10^4 cm^{-3}$ to 4 x $10^5 cm^{-3}$. The molecular structure of CCS, spontaneous decay rates, and collisional rate coefficients are further discussed in the Appendix. The upper levels of observed transitions range from 1.6 K to 20 K above the ground state. Given these parameters, we see that the lower rotational transitions of CCS will be excited only in the relatively dense regions of dark clouds, but together with the higher transitions, they make an effective probe of both temperature and density throughout these regions.

The LVG code requires the collision rate coefficients, A-coefficients and energy levels for a particular molecular species 5'. Line intensities are then calculated for a range of kinetic temperatures, densities, and fractional abundances $X(S) \equiv n(S)/n(H_2)$. The velocity gradient in this code is embedded in the fractional abundances which are entered as the fractional abundance per unit velocity gradient, $X(S)/(dV/dr)$, since the optical depth is proportional to this quantity.

We include the 37 lowest CCS energy levels with their associated collision rates. The line intensities are presented in terms of a *brightness temperature* T_B, defined as the temperature which produces the corresponding Planck function intensity Rayleigh-Jeans limit ($h\nu \ll kT$, i.i.e.

$$T_B = \frac{c^2}{2k\nu^2} I(\nu).$$ (2)

The CCS emission lines used for this study are the $V_J = 1_2 \to 0_1, 3_4 \to 2_3$ and $7_8 \to 6_7$ transitions occurring at approximately 22, 45 and 94 GHz respectively. Figure 1 shows the brightness temperature of the three transitions of interest as a function of H_2 density. The kinetic temperature of the gas is fixed at 10 K and $X(CCS)/(dV/dr)$ is set to 2.5 x $10^{-10} (km s^{-1} pc^{-1})$-', which is the value Fuente et al. (1989) computed for L1498 based On observations and an LVG model. Typical dense core H_2 densities lie in the range $10^4 \to 10^5 cm^{-3}$ (Goldsmith 1987), within the range of the graph. For these particular conditions we see that for most densities, the 45 GHz transition is predicted to be the strongest. For densities above $10^{4.7} cm^{-3}$ the 94 GHz transition should be stronger than the 22 GHz transition. The 45 GHz to 22 GHz line ratio appears to be the most sensitive density tracer at lower densities. The 22 GHz transition becomes optically thick at higher densities than do the other two lines.

Figures 2 - 4 present the brightness temperature of a single Transition together with the ratio of the brightness temperature of two transitions, as a function of n_{H_2} and $X(CCS)/(dV/dr)$ The intersection of these contours allows one to pinpoint the corresponding physical conditions. n_{H_2} and $X(CCS)/(dV/dr)$, in the molecular cloud. We have generated output spanning the range of 7 K to 20 K for use in studies of dark clouds. We present here the intensities and ratios of different transitions for a temperature of 10 K. Results for other temperatures are presented in Wolkovitch (1996).

The contours of constant T_B (thin dashed lines) in Figures 2 to 4 show how the dependence Of T_B on n_{H_2} changes in the sub-thermal and thermal regimes. In the optically thin and sub-thermal regions of the graphs, the brightness temperature is proportional to the product of CCS density and hydrogen density, i.e. $T_B \sim n_{CCS} \cdot n_{H_2} = X(CCS) \cdot (n_{H_2})^2$. Thus for

constant T_B, we expect $X(CCS)/(dV/dr) \sim (n_{H_2})^{-2}$. In the optically thin and thermalized regions of the graph, the brightness temperature depends only on the CCS density, and therefore $T_B \sim n_{CCS} = X(CCS) \cdot n_{H_2}$, and we have $X(CCS)/(dV/dr) \sim (n_{H_2})^{-1}$ The figures show that the slopes Of the constant T_B curves change from -2 to -1 with increasing n_{H_2} as expected.

3. Observations

We employed the 13.6 m Five College Radio Astronomy observatory (FCRAO) telescope in New Salem, MA and the 34 m and 70 m telescopes at NASA's Deep Space Network (DSN) in Goldstone, CA to map two cores. Table 1 contains some relevant telescope and line parameters. All three telescopes had comparable beam sizes, and their spectrometers gave similar velocity resolutions ~ 0.008 $km\,s^{-1}$.

Observations at FCRAO were made in December 1994 and January and June 1995, utilizing the QUARRY 15-element focal plane array (Erickson et al. 1992) and a 1024 channel autocorrelation spectrometer. The 2.5 MHz bandwidth yields channel spacing of 3.0 kHz and a velocity resolution of 0.008 $km\,s^{-1}$ at 94 GHz. We used frequency switching with an offset Of either 0.6 or 0.8 MHz. System temperatures during the observations ranged from 400 K to 650 K In January 1995 we observed Mars and calculated a main beam efficiency of 4.1% at 94 GHz. The 70 m and 34 m DSN telescopes use a 40 MHz, 2 million channel Wide Band Spectrum Analyzer (WBSA), with channels co-added to produce a velocity resolution of 0.008 $km\,s^{-1}$ at 22 GHz. The efficiencies of the 70 m and 34 m dishes have been measured to be 70% and 46% respectively at the frequencies of interest (Langer et al. 1995). The receiver used at the 70 m dish had a maser preamplifier as first stage giving a system temperature of approximately 40 K at 22 GHz. The 34 m antenna was equipped with a cryogenically-cooled HEMT pre-amplifier having a noise temperature of typically 130 K.

3.1. L1498

The central position of L1498, $\alpha(1950) = 04^h07^m50^s.0, \delta(1950) = 25\,°02'13"$, was taken from a CO survey by Myers et al. (1983). This relatively isolated object is located in the Taurus molecular cloud region at an estimated distance of 140 pc. No IRAS sources are associated with this core (Benson & Myers 1989). Observations in various molecules have shown L1498 to be extremely quiescent. For example, Fiebig (1990) reports an NH_3 linewidth of 0.19 $km\,s^{-1}$ and Kuiper, Langer, & Velusamy (1996) report 0.22 $km\,s^{-1}$, only slightly larger than the thermal linewidth of 0.16 $km\,s^{-1}$ at 10 K. Fiebig's observations of the $NH_3(1,1)$ line and the $2_1 - 1_0$ transition of CCS reveal very different spatial distributions for these molecules in L1498, with the NH_3 emission occupying a significantly smaller region than does the CCS. The NH_3 map shows a fairly round, centrally condensed shape to the core, while the CCS map reveals a larger,

slightly elliptical core with two distinct emission peaks, one to the southeast, and one to the west of the ammonia peak. Maps of L1498 have been made in other molecules including $C^{18}O$ (Zhou et al. 1994, Lemme et al. 1995) and CS (Lemme et al. 1995). The morphology of their CS map is similar to that of our CCS maps. Myers et al. (1983) estimated the size of L1498 to be 0.16 pc based on the size of the dark region on the Palomar Atlas Sky Survey, and they placed an upper limit mass on the core of 3.2 $M_\odot$ from CO observations, We used FCRAO to make a 5 X 6 beam-sampled map of L1498 at 94 GHz. The integration time per pointing (which yielded 15 pixels of data) was approximately 5.5 hours. observations of 6 corresponding positions at 15 GHz and 10 corresponding positions at 22 GHz were made with the DSN telescope. Integration times at the DSN were approximately 20 minutes per position. Figure 5 shows CCS spectra at the L1498 central position at all three frequencies.

The CCS lines in L1498 are well fit by a simple gaussian. The linewidths i FWHM) at all positions are remarkably narrcranging from 0.16 to 0.20 $km\ s^1$. At a kinetic temperature of 10 K the C(S thermal linewidth is 0.09 $km\ s^{-1}$, and thus the non-thermal components of the linewidths are between 0.13 and 0.18 $km\ s^{-1}$. Table 2 presents the linewidths and the brightness temperatures at the positions where CCS spectra were observed in more than one transition. The antenna temperatures have been corrected for main beam efficiency. The mean V_{lsr} is 7.85 $km\ s^{-1}$. The linewidths presented are those of the 22 GHz transitions because they have the best signal to noise ratio. The linewidths of the different CCS transitions agree to within the fitting uncertainties at all positions in L1498. Note that the ratios of the peak brightness temperatures vary with position, possibly indicating differences in the physical conditions at each location.

Figure 6 shows a map of integrated intensity of the 94 GHz transition. A comparison of the 94 GHz map to our 22 and 45 GHz maps (see also Kuiper, Langer, & Velusamy 1996), indicates that the core extends less than 50″ beyond of the edge of the map, and displays no distinct structure in this region. The integrated intensity peaks at approximately (80″, -50″), and a weaker peak exists at (-50″. 25″). Our maps are in excellent agreement with Fiebig's CCS ($N_J = 2_1 - - 1_0$) map.

3.2. TMC-1D

We made a 5×6 beam-sampled map of TMC-1 D) at, 94 GHz with a typical integration time of about 8 hours per pointing. 'i'he central position used was $\alpha(1950) = 04^h38^m42^s.0$, $\delta(1950) :.25034'50''$, This map was used with a corresponding; beam-sampled map at 45 GHz, together with a Nyquist-sampled map at 22 GHz (Langer et al. 199<5). We interpolated and convolved th, 22 GHz data to correspond to the positions and spatial resolution of the 45 GHz and 94 GHz spectra. Figures 7 *and* 8 show the 45 GHz *and* 94 GHz spectra (see Langer et al. 1995 for 22 GHz spectra). Figure 9 is a contour map of the total integrated intensity of the three CCS transitions. 'he general shape of TMC-1D looks extremely similar in all three transitions. although the 94 GHz transition appears to be slightly more centrally concentrated.

Unlike the L1498 spectra, the CCS line shapes in TMC-1D are not simple gaussians. Figures 7 and 8 reveal the complexity of the CCS spectra in two transitions, and even more complexity is evident in the Nyquist sampled 22 GHz maps shown in Langer et al. (1995). Possible explanations for the line shapes are self-absorption or multiple distinct velocity components along the line of sight. We may reasonably rule out absorption because the complicated velocity structure appears in all three of the transitions. The present 45 GHz and 94 GHz data strongly suggest, as does the 22 GHz data (Langer et al. 1995), that there are several clumps of gas along the line of sight, each having a slightly different velocity. At least three of these are distinct enough to be analyzed individually. They are located at $V_{LSR} = 5.65$, 5.S9, and 6.11 kms^{-1}, and will be referred co as the low, middle, and high velocity components, respectively,

We have fit each of the spectra with three Gaussian components, A number of attempts indicated that the three intensities, line widths, and central velocities could not all be fit satisfactorily simultaneously. If all 9 parameters were left free, the fitting sometimes produced unreasonably wide or narrow components, and occasionally negative amplitudes. In consequence. we constrained the parameters of the components based on the assumptions that (i) the velocity centroids of each component could not have large velocity displacements across the map; (2) the line widths for all three components had to be similar and larger than the thermal line width for kinetic temperature of 10 K and less than approximately 0.5 km s^{-1}. .-in example of the three gaussian fitting is shown in Figure 10. Further details of the fitting procedure are discussed in Wolkovitch (1996).

4. Determination Of Physical Conditions

We attempted to determine the physical conditions by matching the three line intensities observed with the predictions of the LVG model. We die! this by performing a χ^2 minimization of the difference between our observed line intensities and the predictions of the LVG model. We used the standard definition of χ^2 (Taylor 1982),

$$\chi^2 = \sum_{i}^{n} \left(\frac{T_{B[obs]}(\nu_i) - T_{B[LVG]}(\nu_i)}{\sigma(T_{B[obs]}(\nu_i))} \right)^2 , \tag{3}$$

where $T_{B[obs]}(\nu_i)$ is the observer-1 peak brightness temperature at frequency ν_i, and $T_{B[LVG]}(\nu_i)$ is the corresponding brightness temperature prediction from the LVG code. The standard deviations were taken to be the quadrature sum of the uncertainties in the gaussian line fits and the uncertainties in the telescope efficiencies. The sum in equation 3 is performed over all frequencies observed at the position of interest, The estimated fractional error in main beam efficiency of each telescope is 15%. 'I'his value is based on a typical 10% uncertainty in the temperature of planets used for the calibration and the additional uncertainty of source coupling to the beam. As discussed below, for some positions this minimization approach was successful, while for others there was no clear minimum that would serve to determine the kinetic temperature.

4.1. Kinetic Temperature

4.1.1. L1498

For the six positions at which we observed three CCS transitions, we have made plots of the minimum χ^2 value as a function of temperature, as shown in Figure 11. The plots appear jagged because the χ^2 values were calculated on a discrete grid. The grid intervals for T_K, $\log_{10}(n_{H_2})$, and $\log_{10}(X(CCS)/dV/dr)$ are 1K, 0.05, and 0.05, respectively. At all positions in L1498, the uncertainty in the telescope efficiency is significantly larger than the line fit uncertainties.

'The graphs of χ^2 vs. T_K in Figure 11 display two distinct types of behavior. In three of the six positions, corresponding to the upper plot in Figure 11, the value of χ^2 becomes quite high at lower temperatures, but remains more or less constant at temperatures ranging from 8 K to 20 K, indicating only a lower limit on T_K. In three other positions, seen in the lower plot in Figure 11, the χ^2 values appear to have an overall minimum at or below 7 K. However, the smallest χ^2 values for the positions with a distinct minimum are appreciably larger than the smallest χ^2 values for the positions with only a lower temperature bound. Unfortunately, since we are matching three free parameters to three observations, we are left with no degrees of freedom with which to relate changes in the value of χ^2 to uncertainties in the temperature estimate. Therefore it is not clear how significant are the differences in χ^2. Positions appear to fall into one of two categories in the sense of either having the kinetic temperature well determined with a typical value of 7 K, or of having only a lower limit of approximately 6 K, but allowing solutions up to the maximum value considered of 20 K.

The explanation for this behavior is basically the following. As seen from Figures 2 and 3, the ratios $T_B(45GHz)/T_B(22GHz)$ and $T_B(94GHz)/T_B(22(GHz)$ for any given kinetic temperature T_K are both reasonable probes of the hydrogen density for $10^3 \leq n_{H_2} \leq 10^5$ cm^{-3}. If the density is high, the fractional populations of all of the levels observed are close to being thermalized, and thus relatively independent of the kinetic temperature for $T_K > 7$ K. Thus, we can determine only a lower limit to T_K. Lower densities and subthermal excitation are characterized by smaller values of $T_B(45GHz)/T_B(22GHz)$. In this situation, the fractional population of the upper level of the 94 GHz transition is very sensitive to the kinetic temperature, and we do find a best fit to the observational data for T_K in the range 5 to 8 K.

Although we are not able to determine the kinetic temperature definitively at every position in L1498, the results for the positions with well-defined T_K are consistent with other observations. Benson and Meyers (1989) used NH_3 observations of L1498 to arrive at a temperature of 10.1 K. Fuller and Myers (1993) used observations of a heavy molecule, HC_3N, and a light molecule, NH_3, to separate thermal and non-thermal velocity components of spectral lines. They arrived at a kinetic temperature of 7.7 ± 1.3 K, Fiebig (1990) performed a similar analysis with seven molecular species of varying weights, and arrived at a kinetic temperature of 9.6 ± 1.3 K. However, using a variety of molecular species to determine the temperature in dense cores may be problematic

because of the observed tendency of different molecules to trace different regions within a core (Myers et al. 1991, Swade 1989). This chemical differentiation is also evident in L] 498 (Kuiper et al. 1996) and TMC-1D (Langer et al. 1995).

our results from CCS are consistent with theoretical expectations for a cloud in a well-shielded environment. Calculations balancing the rate of heating and cooling in dense cores (Goldsmith & Langer 1978, Miran 1994) indicate that the heating and cooling mechanisms in molecular clouds place a lower limit of approximately 6 to 8 K on dense core temperatures. In our data half the positions in 1,1498 do not incline towards a particular temperature while the other half indicate temperatures which may be as low as 7 K, Because of this uncertainty, we will adopt a kinetic temperature of 8.5 K throughout L1498, the average between our lowest derived temperature and other evaluations of about 10 K. The dependence of derived density and column density on temperature are discussed in Section 4.2.

4.1.2. TMC-1D

In a manner similar to L1498, we performed a χ^2 minimization to determine the best-fit physical conditions in the velocity components of TMC-1D. The standard deviations were again taken to be the quadrature sum of the fit uncertainties and the telescope calibration uncertainties. The uncertainties in the fits were taken to be the larger of 10% of the brightness temperature and the rms noise. The calibration uncertainties are comparable to the fitting uncertainties in the data. As for 1,1498, the χ^2 minimization was satisfactory only for a fraction of the points observed in TMC-1D. There was no obvious difference in the spatial distribution of these two types of positions. Tölle et al (1981) used NH_3 observations of TMC-1D to estimate a kinetic temperature of 10 ± 1 K. This temperature may not be ideal for assessing our observations because of the tendency of NH_3 and CCS to trace different components of the gas distribution. As for L1498, we will assume a kinetic temperature of 8.5 K.

4.2. H₂ Density and CCS Column Density

4.2.1. L1498

We computed the best-fit values of both n_{H_2} and $X(CCS)/(dV/dr)$ within L1498 by fixing T_K as discussed above and finding the minimum value of χ^2 in 2-dimensional parameter space. There are three different CCS line observations at six positions in 1,1498. Fixing T_K leaves two free parameters in the model, n_{H_2} and $X(CCS)/(dV/dr)$. Since the number of degrees of freedom ν is defined as the number of data points minus the number of free parameters, we were therefore left with' *one* degree of freedom. For $\nu = 1$ the 68% and 95% confidence intervals on χ^2 are $\chi^2 < 1.0$ and $\chi^2 < 3.8$, respectively. Though our techniques are not statistically rigorous due to

the uncertainty in T_K, we will use these confidence intervals as guidelines

Figure 12 shows a typical plot of the χ^2 contours for density and CCS abundance. The slant of the χ^2 ellipse implies that as the best-fit value of n_{H_2} increases, the best-fit $X(CCS)/(dV/dr)$ decreases, and vice-versa, as discussed in Section 2. Table 3 contains the best C-fit densities and CCS column densities at $T_K = 8.5$ K. The best-fit H_2 densities are larger at 7 K than at 8.5 K by factor of $\sim$ 3. The typical density at 10 K is smaller than the density at 8.5 K by a factor of ~ 1.5. Weighting the densities by their χ^2 probabilities and averaging them gives mean volume densities at 7 K, 8.5 K and 10 K of 1.4×10^5, 3.3×10^4 and $2.3 \times 10^4 cm^{-3}$, respectively.

The best-fit CCS column densities change very little with temperature. This insensitivity results from the fact that N(CCS) is proportional to the integrated CCS intensity which is fixed in the χ^2 minimization. The column density in L1498 also remains remarkably constant at different positions. At 8.5 K the weighted mean CCS column density is $6.5 \times 10^{12} cm^{-2}$. Table 4 contains a comparison of this value to other estimates of N(CCS) in L1498. Our value is extremely close to the estimates by Fuente et al. (1990) although it is smaller than Suzuki et al.'s column density by a factor of about 2.5. Figure 6 shows that L1498 may be approximated as an ellipse with a major axis of 0.16 pc, and minor axis Of 0.10 pc, assuming a distance of 140 pc. We may reasonably estimate the line of sight depth of the cloud as the average of these two dimensions, arriving at $D = 0.13$ pc. The fractional abundance of CCS is $N(CCS)/(D\,n_{H_2}) = 4.9 \times 10^{-10}$. This value is smaller by a factor of ~ 16 than the CCS abundance in TMC-1D previously determined by Suzuki et al. (1992) to be 8×10^{-9}, and very similar to the fractional abundance of 4×10^{-10} predicted by Smith et al. (1988) using chemical evolution models of TMC-1D. Another chemical evolution model by Millar and Herbst (1990) predicts a fractional CCS abundance in TMC-1D of 1×10^{-9}

4.2.2. TMC-1D

For TMC-1D, as in L1498, we found the values of $X(CCS)/(dV/dr)$ and n_H, which minimized χ^2 for each position, assuming a temperature of 8.5 K. In computing column densities from the best-fit values of $X(CCS)/(dV/dr)$, we took the velocity linewidth to be the average width of the gaussian components for all three transitions. Figure 13 shows a diagram of the best-fit hydrogen densities superimposed on a contour map of 22 GHz CCS emission from TMC-1D integrated over the appropriate velocity interval corresponding to each component. Our calculated densities vary from 10^3 to $10^6 cm^{-3}$. The very highest densities are somewhat suspect because of the sensitive dependence of the derived density on the 94 GHz line intensity, and the relatively large uncertainty in this quantity. About 80% of the positions in the high- and middle-velocity components have best-fit densities between $10^{3.8}$ and $10^{5.2} cm^{-3}$, and 90% of the positions in the low-velocity component have best-fit densities between $10^{3.0}$ and $10^{4.4} cm^{-3}$. Therefore the low-velocity component of TMC-1D is characterized by a somewhat lower average density than the middle- and high-velocity components.

The average densities in the low (5.65 $km\,s^{-1}$), middle (5.89 $km\,s^{-1}$) and high (6.11 km S^{-1}, velocity components of TMC-1D are computed to be $10^{3.8\pm0.5}$, $10^{4.3\pm0.5}$ and $10^{4.3}\pm0.4$ cm^{-3}, respectively. 'I'able 5 presents a comparison of our values to densities derived by other observers. Our values for the middle and high velocity components seem fairly consistent with previous results, although the low-velocity component has an apparently previously-unrecognized lower density.

We also compare our derived CCS column density to previously obtained values. Because our values of N(CCS) are for the individual velocity components along the line of sight. we may estimate the total column densitv along the line of sight by summing the column densities at the same spatial position. The total column density at the TMC-1D central position is then 3.3×10^{13} cm^{-2}. Table 6 contains 2 comparison of our value to previous estimates of CCS column density in 'I'NIC-1 I). All of the estimates are fairly consistent. Figure 14 overlays the computed column densities on the 22 GHz emission map. There appears to be a significant correspondence between CCS column density and 22 GHz CCS emission.

As for 1,1498, we may estimate the absolute CCS abundance in TMC-1D. While there are three distinct velocity features in TMC-1D, we use the central velocity component for our estimate. as it appears to be the most we]]-defined spatially in Figures 13 and 14. We may approximate the shape of this component by an ellipse with major and minor axes of ~ 0.16 and 0.11 pc, respectively. We will assume the line of sight depth of this component to be the average of the other two dimensions. Then using the column density of the central position of $10^{12.7}\,cm^{-2}$ and the average H_2 density of the central component of $1.9\times10^4\,cm^{-3}$, we obtain a fractional CCS abundance of 5.8×10^{-10}. This value is very close to the X(CCS) determined for L1498 (see Seer, ion 4.2.1.), Our value is also consistent with the predictions of chemical evolution models by Smith et al. (1988) and Millar and Herbst (1990), although our value is significantly smaller than the absolute abundance of 8×10^{-9} derived by Stutzuki et al. (199'2).

5. Discussion

With the density, size, kinetic temperature, and velocity distribution we can estimate the structural and dynamical properties of the dense cores traced by CCS. The general shapes of L1498 and TMC-1D look similar in all three transitions, although the 94 GHz transition appears to be slightly more centrally concentrated. This smaller emission distribution could be due to the higher densities required to excite the $N_J = 7_8$ level.

5.1. Mass Estimates and Virial Equilibrium

Using the size estimates for L1498 from the extent of the CCS emission (see previous section) and the mean density from Table 3, we estimate a mass for L1498 of $2\,M_\odot$ (taking $\mu = 2.33$

amu as the mean mass per particle). We may get a rough idea of whether or not L1198 is gravitationally bound by calculating whether it is in virial equilibrium. In th e simplest scenario, such an equilibrium requires a balance between gravitational potential energy and kinetic energy from thermal and non-thermal motions. MacLaren et al. (1988) show that a self-gravitating sphere with a power law density gradient in virial equilibrium has a mass

$$M_{VT} = k_2 R (\Delta V)^2 \; M_\odot, \tag{4}$$

w h e r e R is the cloud radius in pc, ΔV is the line-of-sight velocity FWHM of an H_2 molecule in $km \, s^{-1}$, and k_2 is a constant which depends on the density gradient. $k_2 = 126$ for $n \propto r^{-2}$, $k_2 = 190$ for $n \propto r^{-1}$ and $k_2 = 210$ for constant n. Equation 4 does not account for the effects of the gas pressure of the surrounding medium.

Before calculating; the virial mass of L1498, we must compute the linewidth of H_2 emission in L1498 because the thermal pressure is provided mainly by the hydrogen. If we assume that CCS is tracing the motions of the bulk of the gas, then the non-thermal portions of the CCS and H_2 linewidths should be the same, and only the thermal motions will differ. Since we know the kinetic temperature of the core, the total H_2 linewidth is

$$\Delta V_{H_2}^2 = 8 ln(2) \cdot \frac{kT}{m_{H_2}} + \Delta V_{NT}^2 = \Delta V_{CCS}^2 + 8 \ln(2) \cdot kT \cdot \left(\frac{1}{m_{H_2}} - \frac{1}{m_{CCS}} \right). \tag{5}$$

From the average CCS linewidth of $0.180 \, km \, s^{-1}$ in L1498, we compute an H_2 linewidth of 0.47 $km \; s^{-1}$ for $T_K = 8.5$ K.

Using equation 4 and assuming; a fairly flat density law $n \propto r^1$, as suggested by the present observations and those of Zhou et al. (1994), we calculate a virial mass of $2.7 M_\odot$ for the L1498 core. Our estimated virial mass is only 30 percent larger than the gravitational mass. L1498 thus appears to be close to virial equilibrium. This analysis is approximate because L1498 does n o t appear to be spherical, however a study by Myers et al. (1991) of dense core s'napes indicates that some elongation of a core does not significantly affect the virial equilibrium estimates. The previous analysis excludes the effects of pressure of the surrounding medium on the core. Only a modest amount of external pressure will result in the core being bound,

The sub-structure seen in Figure 6 could be due to density variations in the core or simply chemical variations. Fiebig (1990) has performed a virial analysis on only the southern "clump" visible in L1498. He estimates a mass of $1.1 M_\odot$ for this clump and finds that the gravitational potential energy is approximately the same as the thermal energy in the cloud. This result is consistent with our calculations. However, there has been a recent suggestion that the two local maxima seen in the 22 GHz CCS emission, one in the northwest and the other in the southeast, are not separate clumps. Instead Kuiper et al, (1996) have proposed that this emission represents limb brightened emission from a shell of CCS. If CCS exists only in a chemical shell then our maps do not trace the central part of the core seen in NH_3 emission by Fiebig (1990). Such a chemical and emission shell would explain our derivation of a relatively constant density over L1498 (see Table 3).

In TM C-1 D we calculate the masses for each of the three different velocity components assuming a cylindrical volume with the diameter given by the width of the CCS 22 GHz emission., 0.1 pc, and the height by the length of the major axis, 0.16 pc. Using the mean density for the low, middle, and high velocity components in Table 5 we find corresponding masses of 0.4, 1.3, and $1.4 M_\odot$. 'The virial masses M_{VT} are calculated using a mean radius $R = 0.06$ pc and ΔV of $0.47\,km\,s^{-1}$. For a constant or slowly varying density profile, consistence with our analysis of TMC-1D), we find M_{VT} about $2.7 M_\odot$. Thus the TMC-1D cores are unbound by factors of 2 to 7. For these cores to remain coherent structures for long times would then require a substantial external pressure, as might be provided by external magnetic fields (cf. Bertoldi and McKee 1992).

5.2. Correlation of N(CCS) with Density

Comparison of column density N(CCS) and volume density n_{H_2} offers a means of investigating variations in hydrogen density together with changes in the fractional abundance of CCS. For TMC-1D) we find a weak inverse correspondence between these quantities. Figure 15 is a log-log plot of derived N versus n_{H_2} for the three velocity components. In these plots we have omitted data points with largest uncertainties. Only the low velocity clump has a statistically meaningful inverse correlation, with linear fit to this plot shows that $N(CCS) \propto 10^{14.1} \cdot n^{-0.22}\,cm^{-2}$. The other two clumps have only weak correlations with $N(CCS) \propto n^{0.07}$, and cannot be distinguished from an essentially flat distribution. This is similar to the result of column density having no or only weak correlation with the density found in Giant Molecular Cloud Cores, using HC_3N to determine density (Bergin et al 1996). one possible explanation for a part of this behavior is our assumption of constant kinetic temperature, For TMC-1D we were unable to determine a kinetic temperature self-consistently from our minimumization analysis and fixed the value at 8.5 K In the analysis here the density solutions are sensitive to the emission intensity of the 94 GHz line which lies about 20 K above the ground state. Thus, modest changes in T_K (111 have fairly large effect on n_{H_2}. If the low N(CCS) regions are slightly warmer than with higher column density, the density calculated here will be lower than the true density, thus flattening what would actually be a modest positive correlation between $N(CCS)$ and $n(H_2)$.

5.3. Filling Factor

The molecular hydrogen densities determined from an excitation analysis of CCS are moderately large for dark cloud cores, 6-30 $\times 10^3 cir1^3$ The fact that these are reasonably close to the mean densities obtained from the virial masses of the dark cloud cores suggests that the filling factor for this gas is not far from unity. This is very different from the low filling factor implied for dense gas in GMC cores (Snell et al. 1994), and imposes significant restrictions on any "clumpy)' model that might be developed to explain the structure of dark cloud cores.

6. Summary

We have undertaken a study to determine the physical conditions in two narrow-line dark cloud cores, L1498 and TMC1-D, using observations of 3 transitions of CCS at comparable spatial resolutions of 0.035 pc, together with an excitation model for CCS.

We computed the CCS-H_2 spin-free collision rates in the close-coupled (CC) approximation. 'These rates represent an improvement over the the OCS-H_2 rates used by other observers to estimate CCS-H_2 collision rates, principally because our rates were calculated in the CC approximation. However, because CCS exhibits intermediate Hund's case coupling, using a method derived in the Hund's case (b) approximation to account for spin-dependence in the rates introduces some Uncertainty into our final rates (see Appendix).

We used a LVG model with our calculated collision rates to predict CCS emission at a variety of kinetic temperatures, densities and CCS abundances, although since the lines observed are not very optically thick, the results should not be highly dependent on the radiative transfer model employed. We found that a combination of three transitions at 22 GHz, 45 GHz and 94 GHz was a good tracer of abundance and density in cores. In a reasonable fraction of positions observed, we were also able to determine fairly accurately the kinetic temperature, while at other positions only a lower limit could be found.

Observations of L1498 reveal it to be an extremely quiescent core with linewidths of --0.19 $km\,s^{-1}$, implying that the non-thermal kinetic energy in the core velocity is only about A third as large as the thermal energy. A map of CCS 94 GHz emission is relatively smooth but with two distinct components within the core. We find that in some positions in the core the best-fit kinetic temperature is approximately 7 K, while at other positions only a lower temperature bound can be (determined. We fixed the kinetic temperature to be 8.5 K inside the core and determined the best-fit molecular hydrogen density and CCS column density at 10 positions in L1498. The density and CCS column density showed only modest variation (typically < factor of two and three, respectively) among these positions. We found an H_2 density of $3.3 \times 10^4\,cm^{-3}$ and an average CCS column density of $6.5 \times 10^{12}\,cm^{-2}$. We estimate a fractional CCS abundance of 4.9x10-10 in L1498. We do not see a significant density variation from edge to center of the condensations we have mapped, which is consistent with a model where CCS emission comes from a uniform shell. The mass estimates of the L1498 core reveal that it is close to virial equilibrium.

Core TMC-1D is comprised of three velocity components along the line of sight centered at approximately 5.65 $km\,s^{-1}$, 5.89 $km\,s^{-1}$, and 6.11 $km\,s^{-1}$. We fit gaussians to the individual components and find them to be extremely quiescent, with linewidths ranging from barely larger than thermal (0.09 $km\,s^{-1}$) to about 0.23 $km\,s^{-1}$. Each component was mapped over a 4' by 5' region, Similarly to the procedure for 1,1498, we fixed the kinetic temperature of the core at 8.5 K, and determined the best-fit H_2 density and CCS column density at 30 positions in each velocity component. The average densities for the three components are 6.3×10^3, 2×10^4 and 2×10^4 cm^{-3}, respectively. The three '(clumps)' in TMC-1D have masses ranging from 0.4 to 1.4 $M_\odot$ and appear

to be gravitationally unbound. As for 1,1498, the H_2 density shows little variation with position in all three velocity components. We estimate a fractional CCS abundance in the central velocity component of $5.8x10^{-10}$.

A. Molecular Structure of CCS

CCS is a symmetric linear molecule with two unpaired spins, producing a total electronic angular momentum $S = 1$. It has no orbital angular momentum $(L = 0)$ and in standard molecular notation of $^{2S+1}\Lambda$, CCS is a $^3\Sigma$ state. Due to its relatively large moment of inertia, $I = 77$ amu·$Å^2$ (Murakami 1990), the rotational levels of CCS are closely spaced, yielding a large number of transitions in the cm and mm bands. The energy level diagram for a $^3\Sigma$ molecule is similar to that of a spin-free linear molecule, but the interaction of spin and rotational angular momenta splits each rotational level into three components. The total angular momentum J is the vector sum Of rotational angular momentum N and spin angular momentum S. The rules of addition for angular momentum allow J to take on any integer value between $J = N + S$ and $J = |N - S|$, inclusive Therefore, for each value of rotational angular momentum N, the total angular momentum may have the values

$$J = N+1, \qquad J = N, \qquad J = N-1 \qquad\qquad (A1)$$

with the exception of the $N = 0$ level which is not split. The three levels in equation A1 are labeled F_1, F_2, and F_3 respectively, and correspond to different projections of S onto the nuclear axis.

A.1. Hund's Cases (a) and (b)

Precise calculation of the energy levels for a molecule with electronic angular momentum can be difficult, because the state energies depend on the strength of the interactions between the various molecular angular momenta (e.g. spin, rotation. orbital). To simplify this problem, Hund developed a classification scheme for linear molecules. based on five idealized molecular models. denoted Hund's cases (a) through (e). The cases are differentia ted by the relative strengths of the coupling of the different molecular angular momenta among each other and with I he internuclear axis of the molecule. Hund's cases are idealizations. and many molecules. including CCS. are hybrids of two or more of these schemes. CCS falls somewhere between Hund's cases (a) and (b). A description these two cases as they apply to the CCS molecule therefore follows. The reader is referred to Townes and Schawlow (1975) for a more general description of Hund's cases.

In the Hund's case (a) model of CCS the strongest coupling is between the electronic angular momentum (due strictly to spin for CCS) and the internuclear axis. The projection of electronic angular momentum S onto the nuclear axis, denoted Σ, is fixed and adds vectorially to the rotational angular momentum operator N to give total angular momentum J. in this idealization, S precesses around the internuclear axis. which in turn precesses around J. Figure 16 diagrams the angular momentum coupling of Hund's case (a).

In Hund's case (b) the coupling is strongest between the spin angular momentum S and the rota.tiol~al angular momentum N. The vector sum of S and N gives the total angular momentum J, whose projection onto the internuclear axis is denoted Ω. Because spin-orbit interaction is usually responsible for the coupling of S to the nuclear axis, molecules like CCS with orbital angular momentum $L = 0$ typically have spin coupled only weakly to the nuclear axis, and therefore Hund's case ('o) is the most appropriate description. In this case, the nuclear axis of the molecule precesses around the vector sum of the spin and rotational angular momenta. as seen in Figure 17.

At high rotational energies. Hund's case (b) is a good representation of CCS. However. for small values of N, coupling between the spin and nuclear axis may be comparable to the coupling or spin and rota tional angular momentum. arid the effects of Hund's case (a) must be taken into account. The determination Of energy levels and line strengths for CCS is a complex undertaking. The transition frequencies and line strengths for CCS and a great many other molecules are available in a molecular line catalog developed at JPL (Pickett et al. 1991). To clarify the characteristics of the transitions we have observed, we show in Figure 18 the energy levels for CCS below approximately 50 K. The computer algorithm used to solve the Hamiltonian of a molecule with spin is described by Pickett (1991). The Einstein .A. -coefficients can be calculated from the line intensities according to the formulas given in the JPL line catalog. Table .-\ l lists the first 60 allowed transitions and thei, Einstein A-coefficients. When using the JPL catalog for calculating CCS transitions or A-coefficients, one should be careful to note that the labels of the $N_J = 2_1$ and 0_1 levels are reversed from those used in this and most other papers. This ambiguity stems from

the fact that N is not a good quantum number at lower rotational energies (cf. Wolkovitch1996)

A.2. Computations

.4.2 .1, Calculation of Collisional Cross Sections

We used a molecular scattering code called Molscat to calculate the CCS-H_2 collisional cross sections. This code was originally written by Dr. S. Green of NASA/GISS, and has been maintained and developed by S. Green and J. Hudson since 1986. It takes as inputs the intermolecular potential and the energy levels and reduced mass of the colliding particles. and computes cross sections. We used this routine 1,0 calculate cross sections in the Close Coupled (CC) approximation.

In a collision of two rigid rotors, the potential depends on the distance between the molecules as well as their relative orientation. One can reduce the parametric dependence of the potential surface in our CCS-H_2 system to only two variables by making two approximations. The first is to treat H_2 as a structureless particle. Since its lowest excited energy state lies above 500 K, collisions] excitation of H_2 is extremely unlikely to occur in a molecular cloud where kinetic energies are of the order of 10 K. The vase majority of H_2 in molecular clouds will be in the lowest energy state. 'The second approximation is to treat CCS as a simple rigid rot, or, neglecting its electronic and vibrational angular momentum. Thus we will obtain state-to-state cross sections only for the spin-free rotational CCS energy levels. Methods for the re-introduction of spin dependence into the collisional cross sections are discussed below. With these two approximations. the potential depends on only the center-of-mass separation R, and the angle between the rotor and a line joining the centers of mass of the two particles.

The intermolecular potential used for the calculations of the cross sections was taken from an ab-initio interaction potential for OCS-H_2 collisions published by Green and Chapman (1978). The potential was tabulated for R in the range $3.0a_0 \leq R \leq 9.5a_0$ at intervals of $0.5a_0$ (a_0 = the Bohr radius), and for 13 equally spaced angles θ where $0° \leq \theta \leq 180°$. A spline interpolation routine, spline.f, provided by S. Green was used to compute the potential at non-gridded points. We accounted for the mass difference between CCS and OCS when entering the reduced mass of the CCS-H_2 system into the scattering code.

Since OCS has $S = 0$, the OCS-H_2 potential could only provide the spin-free rate coefficients Molscat cannot currently compute cross sections fo, spin included energy levels; even if it could, time considerations would make this option unattractive. Including spin effectively triples the number of accessible energy levels of a rotor, and in the CC approximation the computer time required would be nearly two orders of magnitude larger! Methods of including spin in the cross sections. in a more tractable and efficient form are discussed below.

Many different runs were performed at various energies to get a complete sampling of cross

sections to be averaged into the rate coefficients. As the collision energies increased, more and more scattering channels were needed in the computation. We specified the highest rotational state used in the calculation to have higher energy than the kinetic energy of the collision, thus insuring that all open channels were included. Rather than specifying the maximum number of spherical harmonics, 'we let the program run with increasing values Of l until a satisfactory level of convergence was reached. The default tolerances in Molscat are 30% for diagonal matrix elements (corresponding to elastic collisions) and 0.5% for off-diagonal (inelastic collision) matrix elements.

A program to compute the spin-free collision rate coefficients from the collision cross sections, sigrate.f, was also provided by Dr. S. Green. Agreement with detailed balance was checked for the independently-computed upwards anti downwards coefficients. It was found that quite a few of the coefficients did not comply with detailed balance. Agreement was significantly better as the ratio of collision energy to the level spacing between initial and final states increased. The majority of the coefficients agreed to within 20%.

The accuracy of our collision rate coefficients is important for our analysis, but it is difficult to verify the results of a calculation of this kind. In order to check the reasonableness of our coefficients, we compared the spin-free CC S-H_2 collision rate coefficients in the Coupled States (CS) approximation (also supported by Molscat), to the rate coefficients for the OCS-H_2 system published by Green & Chapman (1978). Their rates were computer! in the CS approximation. anti although the rotational constants of OCS differ somewhat from CCS, and the reduced mass of the system is slightly different, we would expect the rates to be similar. A comparison of the two sets of rates reveals that they are extremely similar, with typical differences of less than 10 %. Details of the results and comparison with the Coupled States approximation can be found in Wolkovitch (1995).

A.2.2. Inclusion of Spin Dependence

In this section we discuss two methods of incorporating the effects of spin dependence into collision rates between the pure rotational levels of CCS. The first method, which was the one adopted for our computations, uses the Hund's case (b) approximation to arrive at a scaling formula. 'The second method is more specific to molecules with Hund's case (a) and (b) mixing. but it only allows one to estimate roughly the spin-dependent collision rate coefficients.

A.2.3. IOS Scaling of Rate Coefficients in the Hund's Case (b) Approximation

As mentioned previously, it is easiest to include the spin-rotation interaction in the collision rate coefficients after the spin-free coefficients have been computed. A technique developed by Corey and McCourt(1983) uses the Hund's case "(b) and coupled-states (CS) and infinite order sudden (IOS) approximations to perform this task. Alexander (1982) has performed a similar

REFERENCES

Alexander, M. H. 1982, J. Chem.Phys.,76,3637

Alexander, M. H. & Dagdagain, P. J. 1983, J. Chem.Phys.,79,302.

Beichman, C. A., Myers, P.C.,Emerson,J. P,. Harris, S.,Mathieu.R.. Benson. T . . 1. &Jennings R.E. 1986, ApJ,307,337

Benson, P. J., & Myers, P. C. 1989,ApJS,71,89

Bergin,E.A.,Snell, R. L., and Goldsmith, P.F. 1996, ApJ, 460, 343

Bertoldi, F'., &McKee,C.F.1992,ApJ, 395, 140

Corey, G., & McCourt, F. 1983, J.Phys.Chem,87,2723

Erickson, N. R., Goldsmith, P.F.,Novak,G.,Grosslein.R.M.,Viscuso.P.J.. Erickson. R.B& Predmore, C. R. 1992, IEEE Transactions on Microwave Theory and Techniques.40. !

Fiebig D., 1990, Doktorarbeit,Univ. Bonn (unpublished)

Flower, D., 1990, Molecular Collisions in the Interstellar Medium (Cambridge: Cambridge University Press)

Fuente, i., Cernicharo, J., Barcia. A. & Gomez-Gonzalez. J. 1990, A&A, 231,151

Fuller, G. A.& Myers P. C., 1992,ApJ,384,523

Fuller,G.A. & Myers F', C., 1993.ApJ,418,273

Goldreich, P. & Kwan, J. 1974, ApJ,189,441

Goldsmith, P.F.1987, in Interstellar Processes, ed.D.Hollenbach and H.Thronson (Dordrecht: Reidel), 51

Goldsmith, P. F.&Langer,W.D.1978,ApJ,222,881

Green, S.,& Chapman, S. 1978, ApJS,37,169

Kuiper,T.B.H.,Langer, W. D. & Velusamy,T. 1996, ApJ, in press,

Langer,W. D), Velusamy,T.,Kuiper,T.B.H.,Levin,S.,Olsen,E.&Migenes, V. 1995 ApJ, 453, 293

Lemme, C., Walmsley,C.M.,Wilson, T. I,. & Muders, D.1995,A&A, 302, 509

MacLaren,I., Richardson, K, M.&Wolfendale,A. W. 1988, ApJ, 333, 821

Millar,T.J. &Herbst,E. 1990, A&A, 231, 466

20

calculation to compute rate coefficients in the Hund's case (a) basis

Corey and McCourt develop a formula which uses linear combinations of spin-free cross sections from the ground state to incorporate the spin-rotation interaction into the cross sections. They show that

$$o(NSJ \to N'S'J') = \sum_{\lambda} o_{\lambda}(N,S,J,N',S',J')\, o(0 \to \lambda), \tag{A2}$$

where

$$o_{\lambda}(N,S,J,N',S',J') = [N'NJ] \begin{pmatrix} N' & N & \lambda \\ 0 & 0 & 0 \end{pmatrix}^2 \begin{Bmatrix} \lambda & J & J' \\ S & N' & N \end{Bmatrix}^2. \tag{A3}$$

$S = S' = \frac{1}{2}$ is the spin quantum number. $[x_1...x_n]$ is the product $(2x_1 + 1)...(2x_n + 1)$. The large square and curly brackets denote Wigner 3-j and 6-j symbols respectively (see Rotenberg, 1959). As all of the terms in equation A2 except $o(0 \to \lambda)$ are velocity independent, the same formula may be used for the introduction of spin-rotation interaction to the collision rate coefficients. The cross sections $o(0 \to \lambda)$ are simply replaced with the corresponding rate coefficients, $<o v>_{(0 \to \lambda)}$. This conversion of spin-free to spin-included collision rate coefficients was performed by the program fs_rates.f, written by S. Green. It should be noted that Suzuki et al. (1992) warn against the use of equation A2 for obtaining the spin-included coefficients, saying that the Hund's case (b) approximation overestimates collision rate coefficients between the F_1 and F_2 levels. A discussion of the method they used to compute spin-dependent coefficients follows in the next section.

A.2.4. Scaling of Collision Rates in the Intermediate Coupling Case

Suzuki et al. use a scaling relation from Alexander & Dagdagain (1983) to estimate the spin-included cross sections in terms of cross sections among the pure rotational states. In their paper, Alexander & Dagdagain derive propensity rules for spin-included cross sections in the case of intermediate coupling. Like Corey & McCourt, their calculations are performed in the CS/IOS approximation. Alexander & Dagdagain show that within this approximation the collisional cross section from state F_i in rotational level J, to state F_i' in rotational level J' is given by:

$$o_{JF_i \to J'F_i'} = (2J+1)L_{JF_i}^2 \sum_K A_{JF_i,J'F_i'}^K G^K, \tag{A4}$$

where

$$G^K = \sum_{LL'} (2L+1)(2L'+1) \begin{pmatrix} L' & K & L \\ 0 & 0 & 0 \end{pmatrix}^2 |S_K^L|^2 \tag{A5}$$

and

$$A_{JF_i,J'F_i'}^K = \frac{(2J+1)(2J'+1)}{(2K+1)} \times \left[B_{JF_i,J'F_i'}^K + C_{JF_i,J'F_i'}^K + D_{JF_i,J'F_i'}^K \right]^2 \tag{A6}$$

As before, the large brackets denote a Wigner 3-j symbol. The coefficients B, C and D are defined by Alexander and Dagdagain 1983 in terms of the mixing angles θ_J of the initial and final states

and are straightforward to compute. Unfortunately, computation of the $[SJ_i]$ term is complicated and highly impractical for us to evaluate. However, we may use the fact that G_K is independent of the quantum numbers J and N to reason that the collision rate coefficients between the F_i levels must scale as the value of the coefficients $A^K_{JI_i,J'I'_i}$. Starting with a spin-free cross section between rotational levels J and J' one may roughly approximate the relative strength of the cross sections between the spin-included states by the ratios of the $A^K_{JI_i,J'I'_i}$ terms.

We attempted to use this approximation, but found it to be quite difficult to implement. The magnitude of the $A^K_{JI_i,J'I'_i}$ coefficients appears to vary with K, and it was not clear that arbitrarily taking the ratios of the coefficients for a particular value of K would represent an improvement over the Hund's case (b) IOS scaling approximation discussed in the previous section. If, as Suzuki et al. (1997) claim, collisions between the F_1 and F_2 levels are overestimated by the Hund's case (b) method of the previous section, our predictions of CCS line emission would be in error. However, we were able to use our collision rates to reproduce some of the results presented in Suzuki et al.'s paper.

We present below in Table A2 a key to the numbering of the energy levels of CCS, which is followed by Table A3 containing the CCS H_2 collision rate coefficients at kinetic temperatures of 10K and 20K. These rates have been computed according to the Hund's case (b) method for inclusion of spin discussed above. In the interest of conserving space, only the downwards rates are presented. The labels "i" and "f" in the table refer to the initial and final states of the transition.

Fig. 13.— Log_{10} of the best-fit hydrogen density for the three velocity components in TMC-1D (from left to right, 5.65, 5.89, and $6.11 \, km \, s^{-1}$). Values are overlaid on the contour maps of the 22 GHz brightness temperature integrated over velocity, for each component. Figures in bold font have $\chi^2 < 4$.

Fig. 14.— Log_{10} of the best-fit CCS column density for the three velocity components in TMC-1D (from left to right, 5.65, 5.39, and $6.11 \, km \, s^{-1}$). Figures are overlaid on the contour maps of the 22 GHz peak brightness temperature.

Fig. 15.— Log-log plot of derived N(CCS) versus n_{H_2} in TMC-1D for the three velocity components. Error bars for middle velocity component data have been omitted for clarity.

Fig. 16—— Diagram illustrating Hund's case (a) coupling of N, S, J

Fig. 17.— Diagram illustrating Hund's case ('o) coupling of N, S, J

Fig. 18 .... Energy level diagram for CCS; the states are labeled by the quantum numbers N_J. In this work we observed the $N_J = 1_2 \rightarrow 0_1, 3_4 \rightarrow 2_3$, and $7_8 \rightarrow 6_7$ transitions at frequencies 22.3, 45.4, and 93.9 GHz, respectively.

Table 1. Parameters of CCS Lines and Telescopes

Transition	ν (GHz)	E_u (K)	Telescope	FWHP ($''$)
$1_2 - 0_1$	22.344033	1.61	DSN 70 m	45
$3_4 - 2_3$	45.379031	5.40	DSN 34 m	50
$7_3 - 6_7$	93.870107	19.9	FCRAO	53

-27-

Table 2. ΔV and Peak T_B of CCS Spectra in L1498

Position ('')	ΔV (km/s)	T_B (K) 22 GHz	45 GHz	94 GHz
(0,-100)	0.166(19)	0.411(40)		< 0.062
(0,-50)	0.185(12)	0.943(51)		0.49(10)
(50,-50)	0.181(7)	1.095(30)	2.56(43)	0.96(9)
(100,-50)	0.199(4)	1.303(26)	1.69(47)	1.12(11)
(-50,0)	0.130(7)	1.238(38)	2.46(48)	0.73(9)
(0,0)	0.166(3)	1.453(24)	2.44(50)	0.76(11)
(50,0)	0.160(7)	1.372(50)	1.59(50)	1.07(12)
(100,0)	0.200(11)	1.113(48)		0.52(10)
(-50,50)	0.186(12)	1.064(56)		0.25(10)
(0,50)	0.176(13)	0.992(61)	1.06(54)	0.73(11)

[a] Offsets are relative to the central position. Numbers in parenthesis are 1σ uncertainties in the last digits shown.

Table 3. Best-fit n_{H_2} and $N(CCS)$ in L1498 with $T_K = 8.5$ K

Position (")	$\log_{10}(n_{H_2})$ (cm^{-3})	$\sigma(\log_{10}(n_{H_2}))$ (cm^{-3})		$\log_{10}(N_{CCS})$ (cm^{-2})	$\sigma(\log_{10}(N_{CCS}))$ (cm^{-2})		χ^2
(0,-100)	4.75			12.25			0.27
(0,-50)	4.50			12.66			0.05
(50,-50)	4.75	-0.10	0.15	12.80	-0.20	0.10	0.144
(100,-50)	4.65	-0.20	0.15	12.94	-0.20	0.35	6.42
(-50,0)	4.55	-0.15	0.10	12.79	-0.15	0.20	0.04
(0,0)	4.40	-0.1	0.15	12.86	-0.20	0.10	0.22
(50,0)	4.80	-0.20	0.15	12.74	-0.15	0.25	3.56
(100,0)	4.40			12.79			0.04
(-50,50)	4.15			12.71			0.01
(0,50)	4.80	-0.20	0.15	12.63	-0.15	0.25	3.22

[a] Positions without 1σ error bars on n_{H_2} or $N(CCS)$ were observed in only two CCS transitions

Table 4. Comparison of Derived N(CCS) in L1498

Study	N(CCS) (cm^{-2})
This study	6.5×10^{12}
Fuente et al. (LVG method)	5.6×10^{12}
Fuente et al. (LTE method)	7.0×10^{12}
Suzuki et al.	1.7×10^{13}

Table 5. Comparison of Derived n_{H_2} in TMC-1D

Study	Molecule	n_{H_2} (cm^{-3})
This study (low V_{lsr} component)	CCS	5.6×10^3
This study (middle V_{lsr} component)	CCS	1.9×10^4
This study (high V_{lsr} component)	CCS	2.1×10^4
Suzuki et al.	CCS	$3 - 7 \times 10^4$
Snell et al.	CS	2.0×10^4
Tölle et al.	HC_3N	3×10^4
Hirahara et al.	$C^{34}S$	4.0×10^4
Olano et al.	HC_3N	3×10^4

Table 6. Comparison of Derived N(CCS) in TMC-1D

Study	N(CCS) (cm^{-2})
This study	3.3×10^{13}
Fuente et al (LVG method)	2.3×10^{13}
Fuente et al (LTE method)	2.3×10^{13}
Suzuki et al	6.6×10^{13}
Hirahara et al.	1.0×10^{14}

Table A1. CCS Transitions, Frequencies, and Einstein A-Coefficients

N'_J	N''_J	Frequency (MHz)	A-coefficient (s^{-1})	N'_J	N''_J	Frequency (MHz)	A-coefficient (s^{-1})
2_1	1_1	1855.93	2.9985×10^{-10}	13_{12}	12_{12}	94939.48	3.9968×10^{-7}
3_2	2_2	5402.62	2.5005×10^{-9}	8_7	7_6	99866.52	4.4647×10^{-5}
4_3	3_3	10517.22	8.9966×10^{-9}	8_8	7_7	103640.5	5.0476×10^{-5}
0_1	1_0	11119.48	4.4417×10^{-8}	14_{13}	13_{13}	105347.3	5.5598×10^{-5}
5_4	4_4	16959.29	2.1992×10^{-8}	8_9	7_8	10 362.66	4.7252×10^{-7}
1_2	0_1	22344.03	4.3275×10^{-7}	9_8	8_7	113659.78	6.6263×10^{-5}
6_5	5_5	24506.29	4.2918×10^{-8}	9_9	8_8	117365.64	7.2590×10^{-5}
2_1	1_1	25911.02	5.1087×10^{-7}	15_{14}	14_{14}	118914.64	5.4898×10^{-5}
3_2	2_1	29477.70	7.5263×10^{-7}	8_3	8_9	119814.64	7.8161×10^{-5}
7_6	6_5	32955.97	1.2300×10^{-7}	10_9	9_9	1298.45	9.3609×10^{-5}
2_3	1_2	33753.38	1.5999×10^{-6}	10_{10}	9_9	1293.45	1.0033×10^{-4}
3_3	2_2	38866.42	2.1894×10^{-6}	16_{15}	15_{15}	129719.89	6.2328×10^{-5}
8_7	7_7	42136.09	1.1004×10^{-7}	10_{11}	9_{10}	131551.97	1.0634×10^{-4}
4_5	3_4	43981.03	3.1752×10^{-6}	10_9	10_9	14018.75	1.2731×10^{-4}
3_4	2_3	45379.03	4.0370×10^{-6}	1_{16}	15_{16}	141660.30	7.1035×10^{-5}
4_4	3_3	51321.70	5.6764×10^{-6}	10_{10}	10_{10}	1250.70	1.3435×10^{-4}
9_8	8_8	51305.55	1.5552×10^{-7}	10_{11}	10_{11}	14212.3	1.4078×10^{-4}
4_5	3_4	57229.07	8.2896×10^{-6}	11_{10}	10_{11}	153549.73	1.5800×10^{-4}
5_4	4_3	58253.77	8.0764×10^{-6}	18_{17}	17_{17}	153394.00	7.9476×10^{-5}
10_9	9_9	62151.25	2.0805×10^{-7}	12_{11}	11_{11}	15454.50	1.7529×10^{-4}
5_5	4_4	64776.82	1.1611×10^{-5}	12_{13}	11_{12}	15688.67	1.8198×10^{-4}
5_6	4_5	69281.12	1.4943×10^{-5}	4_3	3_4	157078.23	4.5497×10^{-7}
6_5	5_4	72323.79	1.6184×10^{-5}	5_4	4_5	158112.98	3.6822×10^{-7}
11_{10}	10_{10}	72783.55	2.6671×10^{-7}	3_2	2_3	158476.30	5.5240×10^{-7}
6_5	5_5	77731.71	2.0628×10^{-5}	6_5	5_6	161155.66	2.9995×10^{-7}
6_7	5_6	81505.17	2.4628×10^{-5}	2_1	1_2	162749.95	6.0251×10^{-7}
12_{11}	11_{11}	83731.62	3.3088×10^{-7}	19_{18}	18_{18}	165079.52	8.8108×10^{-5}
7_6	6_5	86181.39	2.8162×10^{-5}	7_6	6_7	165831.86	2.4794×10^{-7}
7_7	6_6	686.38	3.3374×10^{-5}	13_{12}	12_{11}	66662.36	2.1632×10^{-4}
7_8	6_7	93870.11	3.7967×10^{-5}	13_{13}	12_{12}	168406. 0	2.2379×10^{-4}

*Note that the energy levels are denoted N_J and that other authors sometimes use J_N;
See discussion in the Appendix.

Table A2. CCS-H$_2$ Rate Coefficients (units are cm^3 s^{-1})

i	f	Rate Coeff. 10K	Rate Coeff. 20K	i	f	Rate Coeff. 10K	Rate Coeff. 20K	i	f	Rate Coeff. 10K	Rate Coeff. 20K
1	0	4.7E-11	4.3E-11	8	7	2.8E-11	2.9E-11	12	4	2.6E-12	3.6E-12
2	0	2.2E-11	2.3E-11	9	0	1.3E-10	1.2E-10	12	5	3.1E-12	5.3E-12
2	1	1.6E-11	1.5E-11	9	1	3.1E-12	2.9E-11	12	6	7.8E-12	6.4E-12
3	0	1.0E-11	1.0E-11	9	2	1.9E-11	2.1E-11	12	7	1.6E-10	1.4E-10
3	1	2.2E-11	2.1E-11	9	3	5.0E-12	6.0E-12	12	8	3.7E-11	3.5E-11
3	2	4.3E-11	3.6E-11	9	4	8.8E-12	1.3E-11	12	9	1.1E-10	9.3E-11
4	0	2.0E-11	2.2E-11	9	5	2.4E-12	3.9E-12	12	10	8.7E-13	1.8E-12
4	1	3.1E-12	2.9E-12	9	6	4.5E-11	4.0E-11	12	11	1.2E-11	1.2E-11
4	2	6.1E-11	5.6E-11	9	7	1.1E-10	9.0E-11	13	0	0.	0.
4	3	5.6E-11	4.9E-11	9	8	1.7E-11	1.6E-11	13	1	6.4E-12	6.4E-12
5	0	4.4E-12	4.6E-12	10	0	3.7E-12	4.6E-12	13	2	5.6E-12	5.0E-12
5	1	6.4E-12	6.4E-12	10	1	1.4E-12	1.3E-12	13	3	2.3E-11	2.3E-11
5	2	1.1E-11	8.7E-12	10	2	1.9E-11	1.7E-11	13	4	8.5E-12	8.6E-12
5	3	9.2E-11	8.2E-11	10	3	1.6E-11	1.3E-11	13	5	1.3E-11	2.2E-11
5	4	6.8E-11	5.9E-11	10	4	1.0E-10	9.5E-11	13	6	1.2E-11	1.1E-11
6	0	0.	0.	10	5	7.5E-11	6.5E-11	13	7	1.3E-11	1.5E-11
6	1	1.6E-11	1.5E-11	10	6	2.2E-12	2.7E-12	13	8	1.0E-10	8.9E-11
6	2	3.2E-11	3.6E-11	10	7	2.3E-12	2.3E-12	13	9	5.9E-12	6.5E-12
6	3	1.0E-11	1.1E-11	10	8	2.6E-12	2.9E-12	13	10	3.1E-12	4.4E-12
6	4	2.1E-11	2.8E-11	10	9	1.9E-12	3.1E-12	13	11	7.9E-11	6.7E-11
6	5	4.6E-12	6.3E-12	11	0	0.	0.	13	12	1.6E-11	2.0E-11
7	0	1.1E-10	9.4E-11	11	1	3.1E-12	2.9E-12	14	0	2.2E-12	2.1E-12
7	1	2.2E-11	2.1E-11	11	2	2.9E-11	2.3E-11	14	1	1.5E-12	1.4E-12
7	2	9.8E-12	9.5E-12	11	3	1.1E-11	1.1E-11	14	2	4.7E-12	3.8E-12
7	3	3.3E-11	4.2E-11	11	4	2.8E-11	3.3E-11	14	3	2.3E-11	2.6E-11
7	4	5.4E-12	7.3E-12	11	5	4.6E-12	6.0E-12	14	4	2.0E-11	1.7E-11
7	5	6.5E-12	1.1E-11	11	6	7.3E-11	6.8E-11	14	5	1.1E-10	1.1E-10
7	6	2.8E-11	2.4E-11	11	7	6.6E-12	6.6E-12	14	6	1.2E-12	1.2E-12
8	0	0.	0.	11	8	6.7E-11	5.9E-11	14	7	1.4E-12	2.1E-12
8	1	2.2E-11	2.1E-11	11	9	2.3E-11	2.7E-11	14	8	1.9E-12	2.5E-12
8	2	1.6E-11	1.4E-11	11	10	6.0E-12	9.9E-12	14	9	9.3E-13	1.5E-12

Table A2.   (Continued)

i	f	Rate Coeff. 10K	20K	i	f	Rate Coeff. 10K	20K	i	f	Rate Coeff. 10K	20K
8	3	4.7E-11	5.3E-1.	12	0	2.1E-11	1.7E-11	14	10	8.2E-11	7.2E-11
8	4	6.6E-12	7.9E-11	12	1	6.4E-12	6.4E-12	14	11	2.2E-12	2.6E-12
8	5	1.1E-11	1.6E-11	12	2	4.1E-12	4.1E-12	14	12	7.9E-13	1.6E-12
8	6	5.6E-11	4.7E-11	12	3	7.5E-12	9.1E-12	14	13	4.9E-12	6.3E-12
15	0	3.7E-11	3.4E-11	17	4	1.3E-12	1.8E-12	19	4	4.5E-12	4.4E-12
15	1	1.4E-12	1.3E-12	17	5	1.3E-12	2.2E-12	19	5	1.2E-11	1.3E-11
15	2	4.5E-12	5.0E-12	17	6	3.6E-12	2.9E-12	19	6	5.4E-12	4.5E-12
15	3	2.7E-12	3.0E-12	17	7	4.4E-11	4.1E-11	19	7	2.4E-12	2.3E-12
15	4	2.9E-12	4.2E-12	17	8	1.2E-11	1.1E-11	19	8	2.9E-11	2.7E-11
15	5	1.1E-12	1.9E-12	17	9	3.0E-11	2.4E-11	19	9	2.9E-12	3.1E-12
15	6	1.5E-11	1.4E-11	17	10	5.5E-13	1.3E-12	19	10	4.9E-12	5.4E-12
15	7	2.5E-11	2.0E-11	17	11	6.2E-12	5.8E-12	19	11	2.1E-11	1.8E-11
15	8	7.3E-12	6.4E-12	17	12	1.6E-10	1.5E-10	19	12	6.7E-12	8.4E-12
15	9	1.6E-10	1.4E-10	17	13	1.7E-11	1.8E-11	19	13	1.2E-10	1.1E-10
15	10	1.3E-12	2.5E-12	17	14	5.8E-13	1.2E-12	19	14	8.9E-12	1.1E-11
15	11	2.4E-11	2.4E-11	17	15	1.1E-10	9.9E-11	19	15	3.5E-12	4.4E-12
15	12	1.1E-10	9.5E-11	17	16	6.6E-12	7.0E-12	19	16	9.1E-11	7.9E-11
15	13	8.8E-12	8.9E-12	18	0	1.4E-12	1.7E-12	19	17	8.7E-12	1.1E-11
15	14	3.8E-13	1.2E-12	18	1	8.8E-13	6.7E-13	19	18	1.7E-12	2.7E-12
16	0	0.	0.	18	2	4.7E-12	4.2E-12	20	0	8.6E-12	7.7E-12
16	1	1.4E-12	1.3E-12	18	3	7.4E-12	6.0E-12	20	1	8.8E-13	6.7E-13
16	2	8.7E-12	8.6E-12	18	4	3.3E-11	3.2E-11	20	2	1.5E-12	1.7E-12
16	3	5.3E-12	4.9E-12	18	5	2.5E-11	2.1E-11	20	3	1.1E-12	1.3E-12
16	4	1.6E-11	1.7E-11	18	6	7.9E-13	9.7E-13	20	4	1.1E-12	1.7E-12
16	5	6.2E-12	6.6E-12	18	7	7.6E-13	1.1E-12	20	5	6.9E-13	1.3E-12
16	6	2.0E-11	1.9E-11	18	8	1.1E-12	1.3E-12	20	6	3.7E-12	3.3E-12
16	7	2.8E-12	2.9E-12	18	9	5.6E-13	1.2E-12	20	7	1.1E-11	9.0E-12
16	8	1.7E-11	1.4E-11	18	10	1.2E-10	1.1E-10	20	8	3.7E-12	3.2E-12
16	9	9.3E-12	1.1E-11	18	11	1.5E-12	2.2E-12	20	9	4.9E-11	4.5E-11
16	10	1.2E-11	1.5E-11	18	12	4.6E-13	1.2E-12	20	10	6.4E-13	1.1E-12
16	11	1.1E-10	1.0E-10	18	13	1.9E-12	2.4E-12	20	11	8.7E-12	8.8E-12

Table A2.   (Continued)

i	f	Rate Coeff. 10K	20K	i	f	Rate Coeff. 10K	20K	i	f	Rate Coeff. 10K	20K
16	12	4.6E-12	5.4E-12	18	14	9.1E-11	7.8E-11	20	12	3.5E-11	2.8E-11
16	13	8.4E-11	7.3E-11	18	15	3.4E-13	7.5E-13	20	13	5.2E-12	5.1E-12
16	14	2.2E-12	3.4E-12	18	16	3.6E-12	4.8E-12	20	14	2.9E-13	7.3E-13
16	15	1.2E-11	1.4E-11	18	17	2.4E-13	6.7E-13	20	15	1.6E-10	1.5E-10
17	0	8.7E-12	6.9E-12	19	0	0.	0.	20	16	1.2E-11	1.3E-11
17	1	1.5E-12	1.4E-12	19	1	1.5E-12	1.4E-12	20	17	1.2E-10	1.0E-10
17	2	2.0E-12	1.9E-12	19	2	2.7E-12	2.3E-12	20	18	3.0E-13	6.3E-13
17	3	2.3E-12	2.9E-12	19	3	7.6E-12	7.7E-12	20	19	5.2E-12	5.6E-12
21	0	6.1E-13	8.4E-13	22	14	4.0E-12	4.4E-12	24	4	9.7E-12	8.3E-12
21	1	6.7E-13	5.5E-13	22	15	4.8E-12	6.3E-12	24	5	1.1E-11	9.9E-12
21	2	2.2E-12	1.8E-12	22	16	1.3E-10	1.2E-10	24	6	4.0E-13	5.1E-13
21	3	7.5E-12	6.7E-12	22	17	2.8E-12	3.6E-12	24	7	3.5E-13	8.8E-13
21	4	9.5E-12	8.1E-12	22	18	6.8E-12	8.6E-12	24	8	4.3E-13	7.3E-13
21	5	3.8E-11	3.6E-11	22	19	1.0E-10	8.5E-11	24	9	2.0E-13	4.7E-13
21	6	3.4E-13	4.7E-13	22	20	6.7E-12	8.4E-12	24	10	4.2E-11	4.0E-11
21	7	5.7E-13	1.0E-12	22	21	1.3E-12	2.2E-12	24	11	6.5E-13	9.7E-13
21	8	7.7E-13	1.1E-12	23	0	4.1E-12	3.2E-12	24	12	1.6E-13	5.5E-13
21	9	3.6E-13	9.3E-13	23	1	6.7E-13	5.6E-13	24	13	5.1E-13	1.2E-12
21	10	2.8E-11	2.4E-11	23	2	6.3E-13	7.8E-13	24	14	3.4E-11	2.8E-11
21	11	9.6E-13	1.3E-12	23	3	8.8E-13	1.2E-12	24	15	1.1E-13	2.9E-13
21	12	2.2E-13	5.4E-13	23	4	5.9E-13	1.1E-12	24	16	9.8E-13	1.5E-12
21	13	1.2E-12	1.8E-12	23	5	5.3E-13	8.7E-13	24	17	1.3E-13	3.7E-13
21	14	1.2E-10	1.2E-10	23	6	1.8E-12	1.4E-12	24	18	1.3E-10	1.2E-10
21	15	2.2E-13	6.7E-13	23	7	1.1E-11	1.0E-11	24	19	1.4E-12	1.9E-12
21	16	1.5E-12	2.1E-12	23	8	3.5E-12	3.3E-12	24	20	9.9E-14	2.1E-13
21	17	1.7E-13	4.0E-13	23	9	1.3E-11	1.1E-11	24	21	1.1E-10	9.0E-11
21	18	9.7E-11	8.4E-11	23	10	3.7E-13	8.1E-13	24	22	2.2E-12	3.1E-12
21	19	2.7E-12	3.7E-12	23	11	3.2E-12	3.0E-12	24	23	3.6E-14	2.1E-13
21	20	1.3E-13	3.6E-13	23	12	5.1E-11	4.9E-11	25	0	0.	0.
22	0	0.	0.	23	13	6.6E-12	7.0E-12	25	1	6.7E-13	5.6E-13
22	1	8.8E-13	6.7E-13	23	14	3.4E-13	6.0E-13	25	2	1.2E-12	1.1E-12

–36–

Table A2. (Continued)

i	f	Rate Coeff. 10K	20K	i	f	Rate Coeff. 10K	20K	i	f	Rate Coeff. 10K	20K
22	2	2.5E-12	2.4E-12	23	15	3.7E-11	3.2E-11	25	3	2.5E-12	2.5E-12
22	3	2.6E-12	2.4E-12	23	16	4.2E-12	4.4E-12	25	4	2.3E-12	2.3E-12
22	4	6.1E-12	6.4E-12	23	17	1.6E-10	1.5E-10	25	5	4.8E-12	5.2E-12
22	5	3.9E-12	4.0E-12	23	18	1.7E-13	4.0E-13	25	6	2.3E-12	2.0E-12
22	6	5.0E-12	4.7E-12	23	19	9.0E-12	1.0E-11	25	7	9.2E-13	1.1E-12
22	7	1.4E-12	1.4E-12	23	20	1.2E-10	1.1E-10	25	8	7.6E-12	7.0E-12
22	8	7.5E-12	6.2E-12	23	21	1.7E-13	3.4E-13	25	9	1.3E-12	1.4E-12
22	9	2.1E-12	2.7E-12	23	22	4.2E-12	4.6E-12	25	10	3.2E-12	3.5E-12
22	10	9.1E-12	9.9E-12	24	0	7.2E-13	9.3E-13	25	11	9.6E-12	8.3E-12
22	11	3.6E-11	3.3E-11	24	1	4.0E-13	3.2E-13	25	12	1.6E-12	2.3E-12
22	12	2.5E-12	2.9E-12	24	2	2.3E-12	1.8E-12	25	13	4.0E-11	3.8E-11
22	13	2.6E-11	2.2E-11	24	3	4.3E-12	3.4E-12	25	14	6.9E-12	7.7E-12
25	15	2.0E-12	2.6E-12	26	25	3.6E-12	3.9E-12	28	7	2.0E-13	3.9E-13
25	16	3.0E-11	2.5E-11	27	0	0.	0.	28	8	3.7E-13	5.2E-13
25	17	3.5E-12	4.3E-12	27	1	4.0E-13	3.2E-13	28	9	1.4E-13	5.4E-13
25	18	3.3E-12	3.7E-12	27	2	1.2E-12	1.1E-12	28	10	1.3E-11	1.1E-11
25	19	1.3E-10	1.2E-10	27	3	1.4E-12	1.4E-12	28	11	3.6E-13	7.6E-13
25	20	2.3E-12	3.0E-12	27	4	2.2E-12	2.3E-12	28	12	9.0E-14	2.6E-13
25	21	5.3E-12	6.7E-12	27	5	2.0E-12	2.1E-12	28	13	5.4E-13	8.5E-13
25	22	1.1E-10	9.1E-11	27	6	2.4E-12	2.0E-12	28	14	4.4E-11	4.3E-11
25	23	5.3E-12	6.7E-12	27	7	4.8E-13	6.2E-13	28	15	7.9E-14	2.7E-13
25	24	1.1E-12	1.8E-12	27	8	4.4E-12	3.7E-12	28	16	6.8E-13	1.0E-12
26	0	4.0E-12	3.1E-12	27	9	8.7E-13	1.2E-12	28	17	5.9E-14	1.5E-13
26	1	4.0E-13	3.2E-13	27	10	4.0E-12	4.3E-12	28	18	3.6E-11	3.0E-11
26	2	7.6E-13	8.3E-13	27	11	9.8E-12	8.8E-12	28	19	8.0E-13	1.2E-12
26	3	5.3E-13	9.4E-13	27	12	1.1E-12	1.4E-12	28	20	7.7E-14	2.0E-13
26	4	4.3E-13	6.9E-13	27	13	1.2E-11	1.0E-11	28	21	1.3E-10	1.2E-10
26	5	3.2E-13	6.9E-13	27	14	3.0E-12	3.1E-12	28	22	1.2E-12	1.6E-12
26	6	1.8E-12	1.4E-12	27	15	1.3E-12	1.9E-12	28	23	6.1E-14	1.3E-13
26	7	6.6E-12	5.0E-12	27	16	4.5E-11	4.2E-11	28	24	1.1E-10	9.3E-11
26	8	2.0E-12	1.7E-12	27	17	1.8E-12	2.3E-12	28	25	1.8E-12	2.5E-12

Table A.2 . (Continued)

i	f	Rate Coeff. 10K	20K	i	f	Rate Coeff. 10K	20K	i	f	Rate Coeff. 10K	20K
26	9	1.3E-11	1.2E-11	27	18	5.7E-12	6.3E-12	28	26	5.6E-14	1.3E-13
26	10	3.0E-13	5.0E-13	27	19	3.6E-11	2.9E-11	28	27	1.4E-12	1.8E-12
26	11	3.0E-12	3.0E-12	27	20	2.8E-12	3.8E-12	29	0	3.3E-12	2.1E-12
26	12	1.5E-11	1.3E-11	27	21	2.9E-12	3.2E-12	29	1	4.0E-13	3.3E-13
26	13	2.7E-12	2.7E-12	27	22	1.4E-10	1.3E-10	29	2	7.2E-13	8.6E-13
26	14	2.4E-13	4.3E-13	27	23	2.0E-12	2.6E-12	29	3	4.1E-13	5.4E-13
26	15	5.5E-11	5.2E-11	27	24	4.3E-12	5.4E-12	29	4	2.9E-13	6.5E-13
26	16	5.2E-12	5.6E-12	27	25	1.2E-10	9.7E-11	29	5	2.4E-13	4.2E-13
26	17	4.4E-11	3.6E-11	27	26	4.2E-12	5.4E-12	29	6	1.5E-12	9.6E-13
26	18	2.1E-13	3.4E-13	28	0	7.3E-13	1.1E-12	29	7	5.7E-12	4.3E-12
26	19	3.8E-12	3.9E-12	28	1	4.0E-13	3.3E-13	29	8	1.9E-12	1.6E-12
26	20	1.6E-10	1.5E-10	28	2	1.9E-12	1.3E-12	29	9	8.1E-12	6.4E-12
26	21	1.1E-13	2.4E-13	28	3	3.9E-12	3.0E-12	29	10	1.3E-13	3.3E-13
26	22	7.2E-12	7.9E-12	28	4	5.8E-12	4.7E-12	29	11	1.8E-12	1.8E-12
26	23	1.3E-10	1.1E-10	28	5	1.1E-11	1.1E-11	29	12	1.5E-11	1.4E-11
26	24	1.1E-13	2.1E-13	28	6	4.0E-13	5.8E-13	29	13	2.5E-12	2.6E-12
29	13	2.5E-12	2.6E-12	30	19	4.7E-11	4.5E-11	31	24	1.3E-10	1.3E-10
29	14	1.8E-13	2.3E-13	30	20	1.4E-12	1.9E-12	31	25	9.1E-13	1.3E-12
29	15	1.7E-11	1.4E-11	30	21	4.7E-12	5.2E-12	31	26	4.0E-14	8.4E-14
29	16	2.2E-12	2.3E-12	30	22	3.8E-11	3.1E-11	31	27	1.5E-12	2.1E-12
29	17	5.6E-11	5.4E-11	30	23	2.2E-12	3.1E-12	31	28	1.1E-10	9.4E-11
29	18	1.5E-13	2.7E-13	30	24	2.5E-12	2.7E-12	31	29	3.6E-14	8.7E-14
29	19	4.1E-12	4.5E-12	30	25	1.4E-10	1.3E-10	31	30	1.1E-12	1.5E-12
29	20	4.5E-11	3.7E-11	30	26	1.6E-12	2.1E-12	32	0	2.0E-12	1.7E-12
29	21	1.3E-13	2.2E-13	30	27	1.2E-10	1.0E-10	32	1	3.3E-13	3.3E-13
29	22	3.0E-12	3.2E-12	30	28	3.5E-12	4.5E-12	32	2	2.7E-13	3.2E-13
29	23	1.6E-10	1.5E-10	30	29	3.5E-12	4.4E-12	32	3	4.1E-13	7.1E-13
29	24	7.3E-14	1.5E-13	31	0	1.9E-13	3.1E-13	32	4	1.8E-13	3.2E-13
29	25	5.7E-12	6.4E-12	31	1	3.3E-13	3.3E-13	32	5	1.5E-13	3.4E-13
29	26	1.4E-10	1.1E-10	31	2	1.1E-12	9.5E-13	32	6	9.2E-13	7.6E-13
29	27	3.0E-12	3.3E-12	31	3	3.1E-12	2.3E-12	32	7	4.6E-12	3.2E-12
29	28	7.1E-14	1.4E-13	31	4	4.2E-12	3.7E-12	32	8	1.6E-12	1.4E-12

Table A2. (Continued)

i	f	Rate Coeff. 10K	Rate Coeff. 20K	i	f	Rate Coeff. 10K	Rate Coeff. 20K	i	f	Rate Coeff. 10K	Rate Coeff. 20K
30	0	0.	0.	31	5	6.3E-12	5.5E-12	32	9	5.8E-12	5.0E-12
30	1	4.0E-13	3.3E-13	31	6	1.0E-13	1.7E-13	32	10	1.3E-13	2.2E-13
30	2	1.1E-12	9.1E-13	31	7	2.4E-13	6.2E-13	32	11	1.3E-12	1.4E-12
30	3	1.3E-12	1.2E-12	31	8	3.9E-13	5.8E-13	32	12	8.4E-12	1.1E-12
30	4	1.3E-12	1.5E-12	31	9	6.6E-14	2.0E-13	32	13	1.4E-12	1.6E-12
30	5	1.8E-12	2.0E-12	31	10	1.2E-11	1.1E-11	32	14	1.1E-12	2.1E-12
30	6	2.0E-12	1.6E-12	31	11	2.7E-13	2.4E-13	32	15	1.5E-11	1.5E-11
30	7	4.9E-13	6.1E-13	31	12	5.5E-14	6.5E-13	32	16	1.8E-12	2.1E-12
30	8	3.3E-12	2.9E-12	31	13	3.0E-13	4.4E-13	32	17	1.7E-11	1.8E-11
30	9	5.0E-13	8.6E-13	31	14	4.6E-14	1.2E-13	32	18	1.1E-13	1.5E-13
30	10	1.7E-12	1.9E-12	31	15	4.5E-13	4.5E-13	32	19	1.3E-12	1.9E-12
30	11	5.9E-12	4.3E-12	31	16	4.4E-14	1.4E-13	32	20	3.6E-11	5.5E-11
30	12	7.1E-13	1.1E-12	31	17	4.4E-14	1.4E-13	32	21	8.9E-14	1.7E-13
30	13	1.2E-11	1.1E-11	31	18	4.1E-13	6.9E-13	32	22	3.3E-12	3.7E-12
30	14	3.3E-12	3.6E-12	31	19	3.6E-13	8.5E-13	32	23	4.2E-11	3.7E-11
30	15	8.7E-13	1.2E-12	31	20	3.5E-14	8.5E-13	32	24	8.8E-14	1.8E-13
30	16	1.3E-11	1.1E-11	31	21	3.5E-11	5.0E-14	32	25	2.4E-12	2.6E-12
30	17	1.0E-12	1.5E-12	31	22	6.5E-13	5.0E-12	32	26	1.5E-10	1.5E-10
30	18	2.5E-12	2.5E-12	31	23	4.6E-14	1.2E-13	32	27	4.7E-12	5.3E-12
30	19	4.7E-11	4.5E-11	31	24	1.3E-10	1.3E-10	32	28	4.7E-14	1.0E-13
32	29	1.3E-10	1.1E-10	31	32	2.9E-12	3.7E-12	35	0	2.4E-12	2.0E-12
32	30	2.3E-12	2.7E-12	34	0	3.1E-13	5.5E-13	35	1	1.5E-13	1.3E-13
32	31	4.8E-14	9.1E-14	34	1	1.5E-13	1.3E-13	35	2	3.9E-13	5.1E-13
33	0	0.	0.	34	2	1.4E-12	1.2E-12	35	3	1.7E-13	2.7E-13
33	1	3.3E-13	3.3E-13	34	3	2.1E-12	1.7E-12	35	4	1.8E-13	3.7E-13
33	2	5.7E-13	5.2E-13	34	4	3.5E-12	3.0E-12	35	5	1.1E-13	1.7E-13
33	3	1.1E-12	1.1E-12	34	5	5.2E-12	4.6E-12	35	6	1.1E-12	9.2E-13
33	4	9.9E-13	1.0E-12	34	6	1.7E-13	2.9E-13	35	7	3.1E-12	2.5E-12
33	5	1.1E-12	1.3E-12	34	7	6.7E-14	1.9E-13	35	8	9.6E-13	8.3E-13
33	6	1.1E-12	9.8E-13	34	8	1.1E-13	2.1E-13	35	9	4.8E-12	3.9E-12
33	7	4.8E-13	7.2E-13	34	9	7.1E-14	2.5E-13	35	10	7.8E-14	1.8E-13

Table A2 (Continued).

i	f	Rate Coeff. 10K	Rate Coeff. 20K	i	f	Rate Coeff. 10K	Rate Coeff. 20K	i	f	Rate Coeff. 10K	Rate Coeff. 20K
33	8	3.0E-12	2.3E-12	34	10	6.3E-12	5.7E-12	35	11	1.2E-12	1.3E-12
33	9	3.6E-13	5.5E-13	34	11	2.3E-13	5.8E-13	35	12	6.3E-12	6.0E-12
33	10	1.4E-12	1.7E-12	34	12	2.9E-14	8.1E-14	35	13	1.2E-12	1.2E-12
33	11	4.2E-12	3.6E-12	34	13	2.3E-13	4.0E-13	35	14	8.6E-14	1.4E-13
33	12	3.9E-13	7.9E-13	34	14	1.3E-11	1.3E-11	35	15	8.1E-12	7.2E-12
33	13	6.5E-12	5.3E-12	34	15	2.6E-14	1.0E-13	35	16	1.0E-12	1.3E-12
33	14	1.4E-12	1.6E-12	34	16	2.2E-13	5.1E-13	35	17	1.5E-11	1.6E-11
33	15	5.3E-13	8.7E-13	34	17	2.5E-14	6.6E-14	35	18	6.7E-14	1.3E-13
33	16	1.2E-11	1.2E-11	34	18	1.4E-11	1.2E-11	35	19	1.6E-12	1.8E-12
33	17	6.9E-13	1.0E-12	34	19	3.6E-13	6.1E-13	35	20	1.7E-11	1.5E-11
33	18	2.7E-12	3.0E-12	34	20	2.5E-14	7.8E-14	35	21	7.9E-14	1.2E-13
33	19	1.4E-11	1.2E-11	34	21	4.9E-11	4.7E-11	35	22	1.4E-12	1.6E-12
33	20	8.0E-13	1.2E-12	34	22	4.4E-13	6.9E-13	35	23	6.0E-11	5.7E-11
33	21	1.9E-12	2.2E-12	34	23	2.4E-14	5.6E-14	35	24	5.3E-14	1.1E-13
33	22	4.8E-11	4.7E-11	34	24	3.4E-11	3.1E-11	35	25	2.9E-12	3.1E-12
33	23	1.1E-12	1.6E-12	34	25	5.7E-13	8.3E-13	35	26	4.1E-11	3.7E-11
33	24	3.9E-12	4.4E-12	34	26	2.9E-14	7.7E-14	35	27	1.9E-12	2.2E-12
33	25	3.7E-11	3.1E-11	34	27	7.4E-13	1.1E-12	35	28	6.6E-14	1.0E-13
33	26	1.8E-12	2.5E-12	34	28	1.4E-10	1.3E-10	35	29	1.7E-10	1.6E-10
33	27	1.4E-10	1.4E-10	34	29	2.9E-14	5.9E-14	35	30	4.2E-12	4.6E-12
33	28	2.0E-12	2.3E-12	34	30	1.4E-12	1.9E-12	35	31	3.5E-14	7.3E-14
33	29	1.3E-12	1.8E-12	34	31	1.2E-10	9.9E-11	35	32	1.4E-10	1.2E-10
33	30	1.2E-10	1.0E-10	34	32	2.6E-14	6.2E-14	35	33	2.1E-12	2.3E-12
33	31	2.9E-12	3.7E-12	34	33	9.6E-13	1.3E-12	35	34	3.4E-14	6.4E-14
36	0	0.	0.	36	12	3.0E-13	5.1E-13	36	24	1.6E-12	1.8E-12
36	1	1.5E-13	1.3E-13	36	13	5.3E-12	4.6E-12	36	25	5.2E-11	5.0E-11
36	2	7.3E-13	7.0E-13	36	14	1.3E-12	1.5E-12	36	26	8.3E-13	1.3E-12
36	3	6.5E-13	6.2E-13	36	15	2.8E-13	6.4E-13	36	27	3.6E-11	3.2E-11
36	4	8.9E-13	1.0E-12	36	16	6.6E-12	5.6E-12	36	28	3.6E-12	3.9E-12
36	5	8.9E-13	9.6E-13	36	17	4.5E-13	7.5E-13	36	29	1.7E-12	2.2E-12
36	6	1.4E-12	1.3E-12	36	18	1.1E-12	1.3E-12	36	30	1.5E-10	1.4E-10

#		N_j	#		N_j	#		N_j	#		N_j
0	←	1_0	10	→	5_5	20	←	7_8	30	←	10_{10}
1	←	0_1	11	→	3_3	21	←	8_9	31	←	11_{12}
2	→	1_2	12	←	4_3	22	←	7_7	32	←	11_{10}
3	←	2_3	13		4_4	23	←	8_7	33	←	11_{11}
4	←	3_4	14	←	6_7	24	←	9_{10}	34	←	12_{13}
5	←	4_5	15	→	5_4	25	←	8_8	35	→	12_{11}
6	←	1_1	16	←	5_5	26	→	9_8	36	←	12_{12}
7	→	2_1	17	←	6_5	27	→	9_9			
8	→	2_2	18	→	7_8	28	←	10_{11}			
9	→	3_2	19	→	6_6	29	→	10_9			

Figure 1

$T_k = 10$ K

$\log_{10} X(\ CCS)/(dV/dR) = -9.60$ (pc/(km s^{-1}))

T_B K)

22 GHz

45 GHz

94 GHz

$\log_{10} n(H_2)$ (c m - 3)
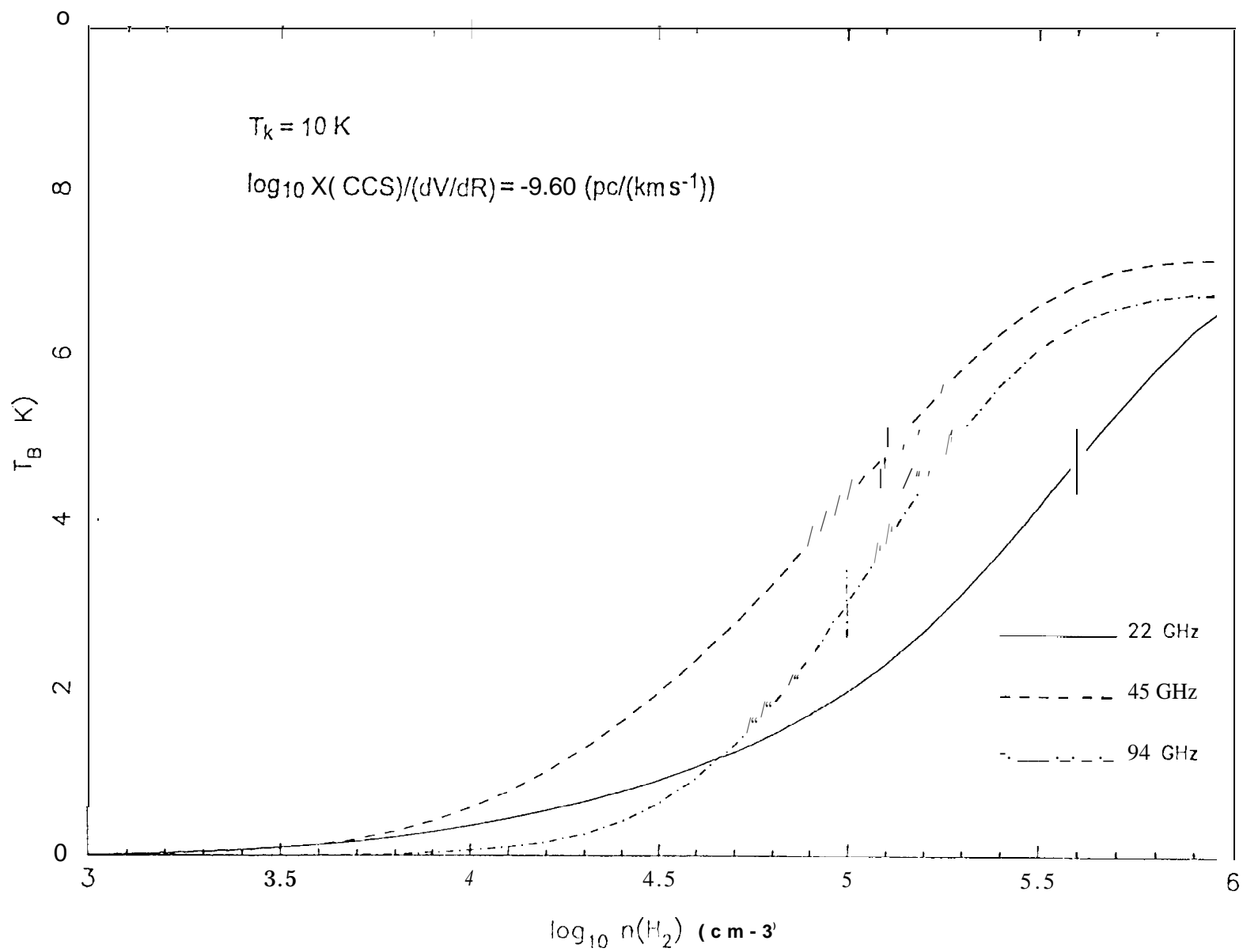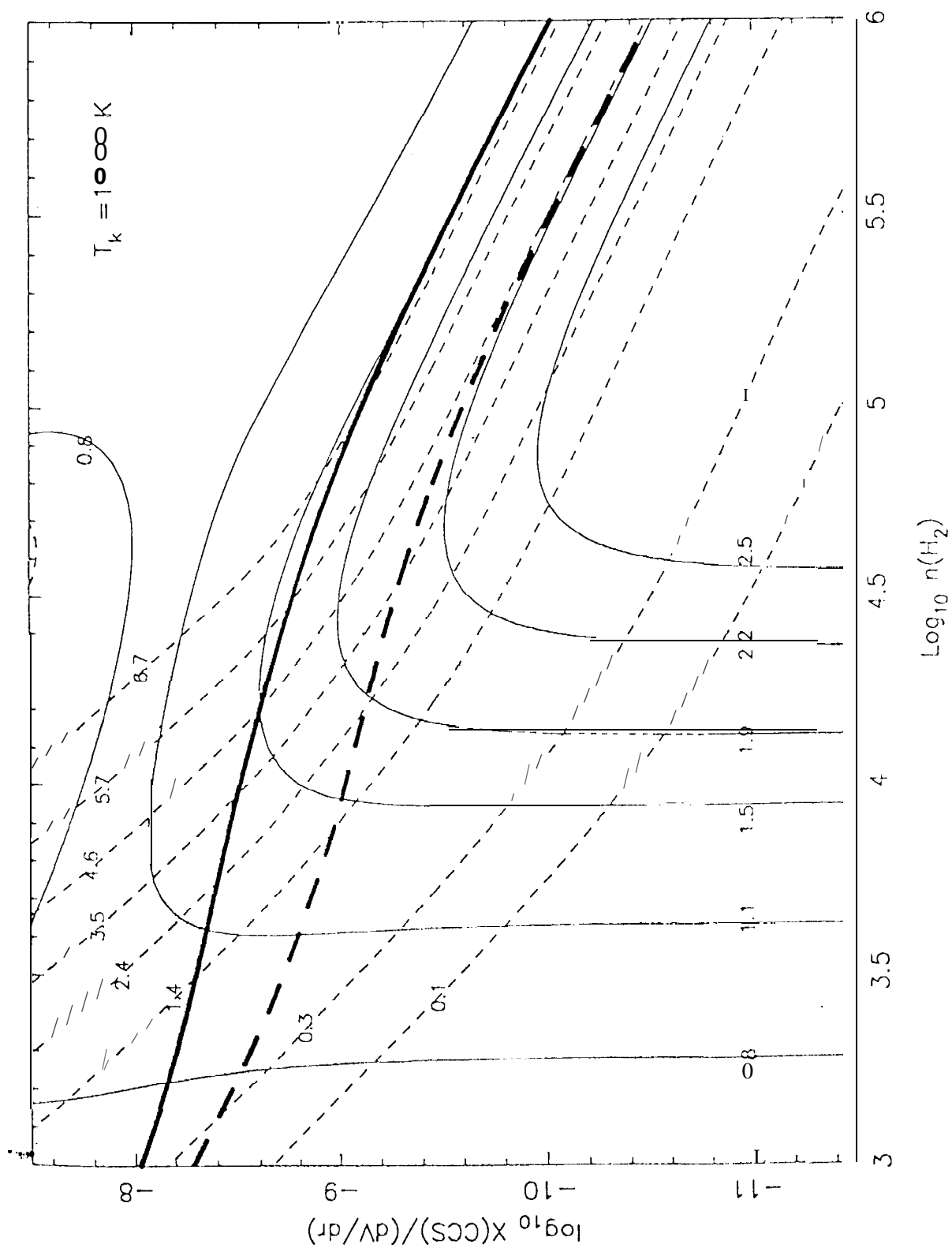
Figure 2

Figure 3

Figure 4

Antenna Temperature (K)

Velocity (km/s)

45 GHz

22 GHz

94 GHz

Figure 6

(0,0)

T_B (K)

V_{lsr} (km/s)
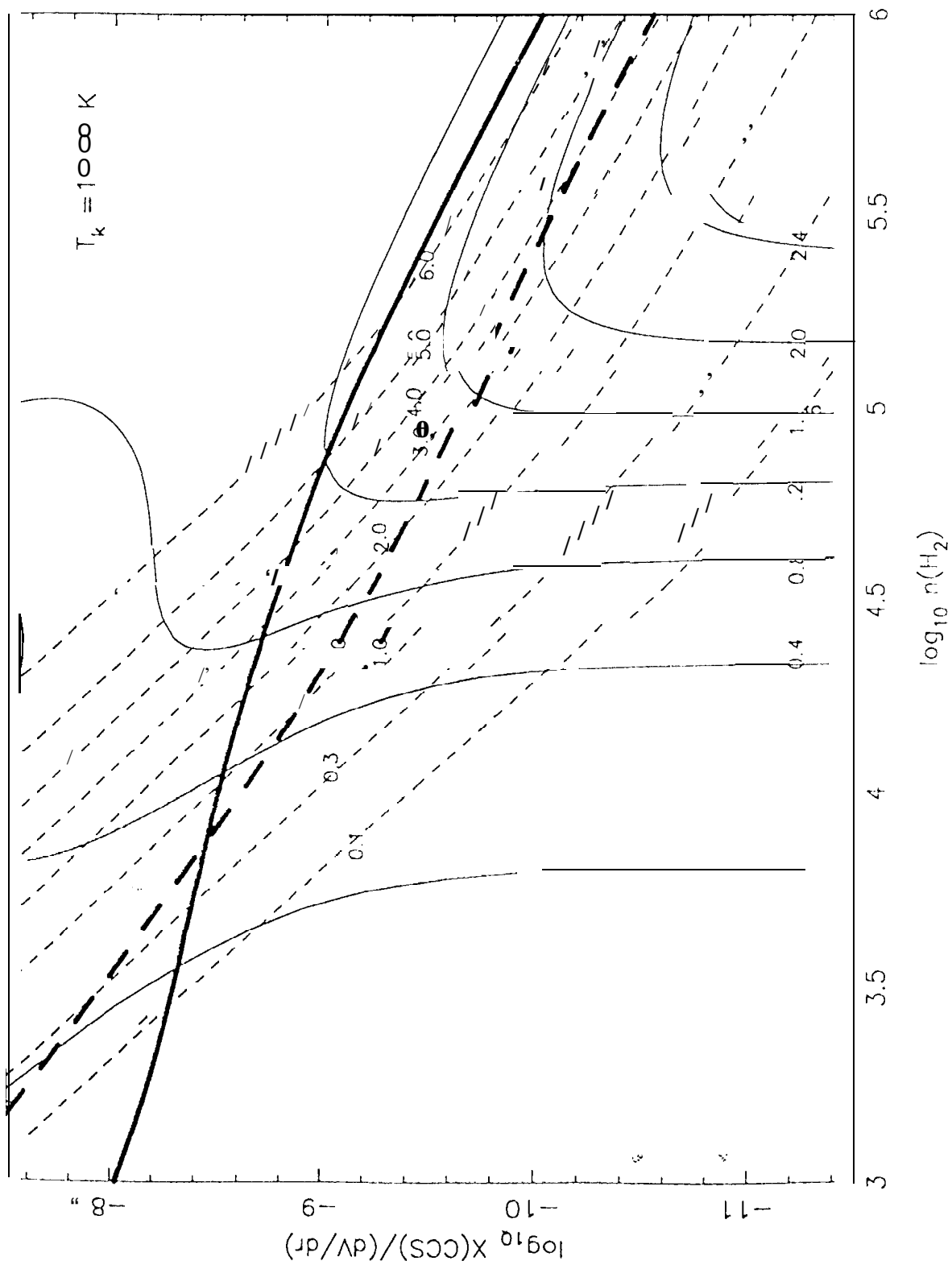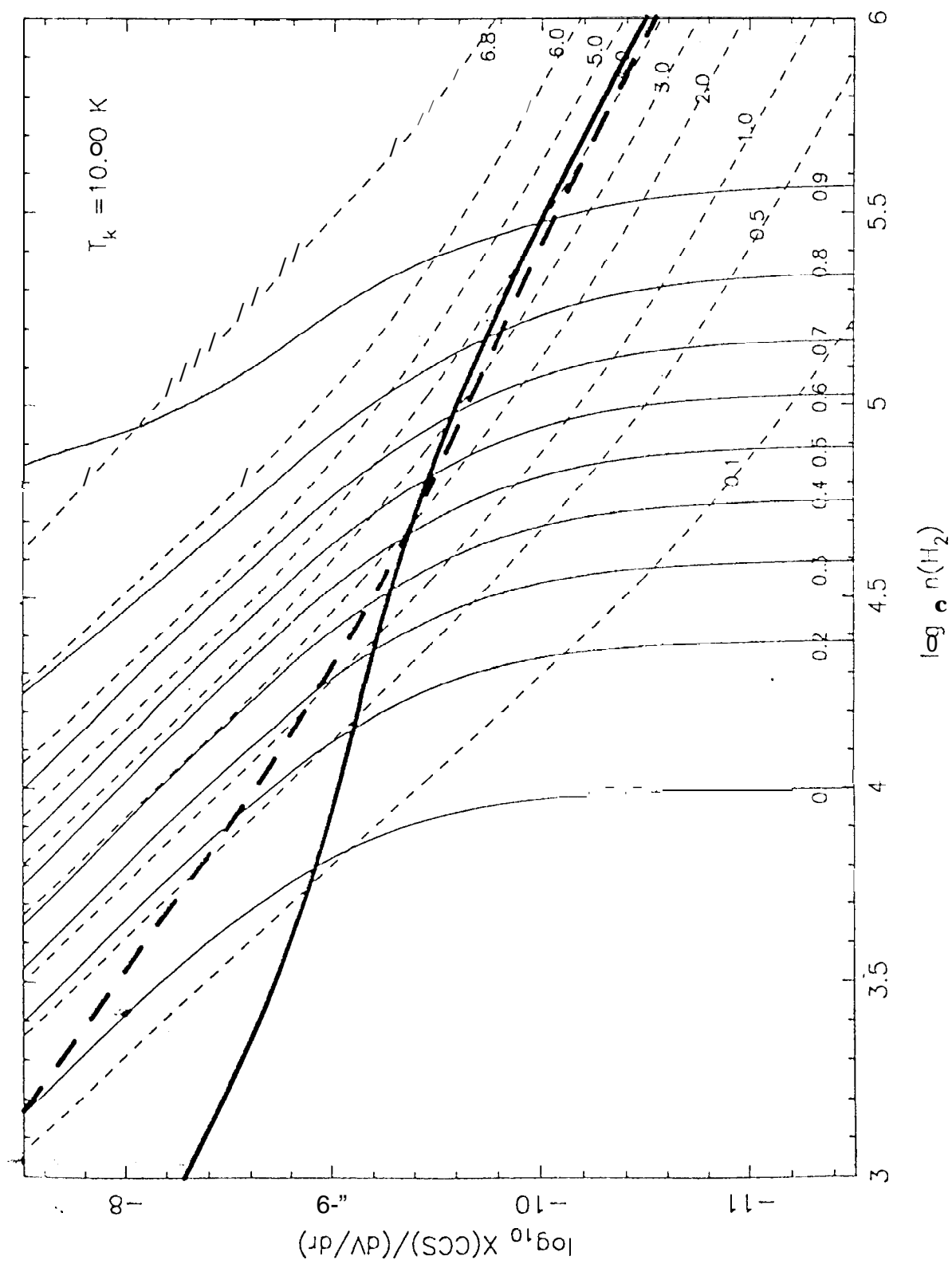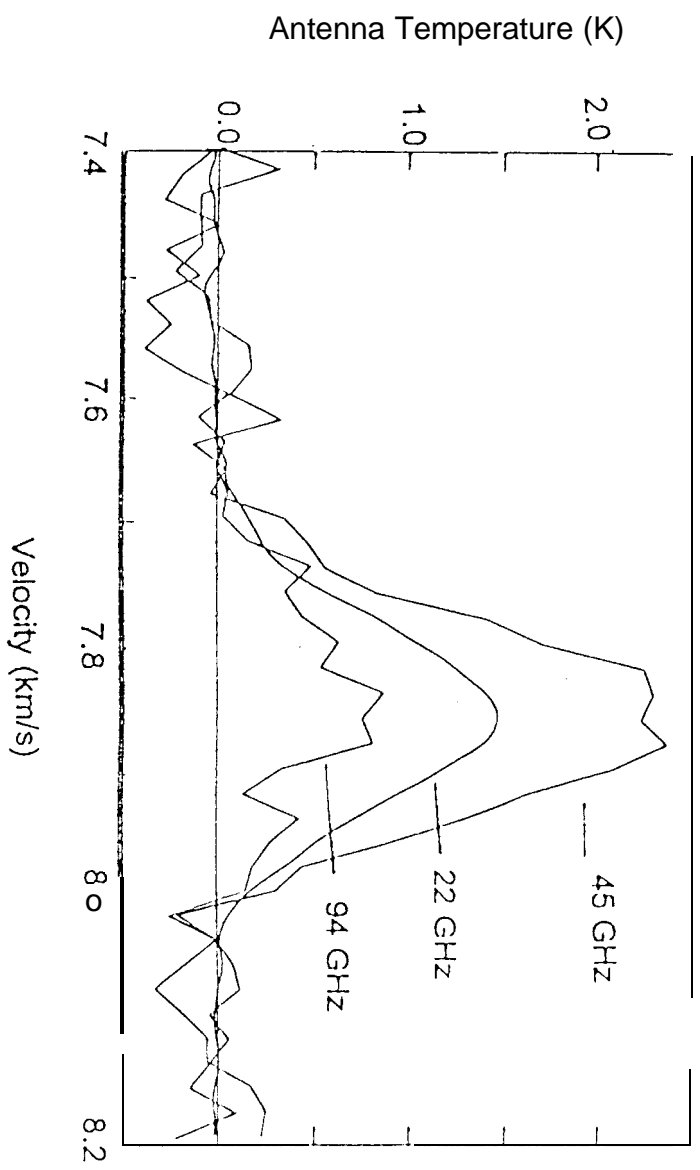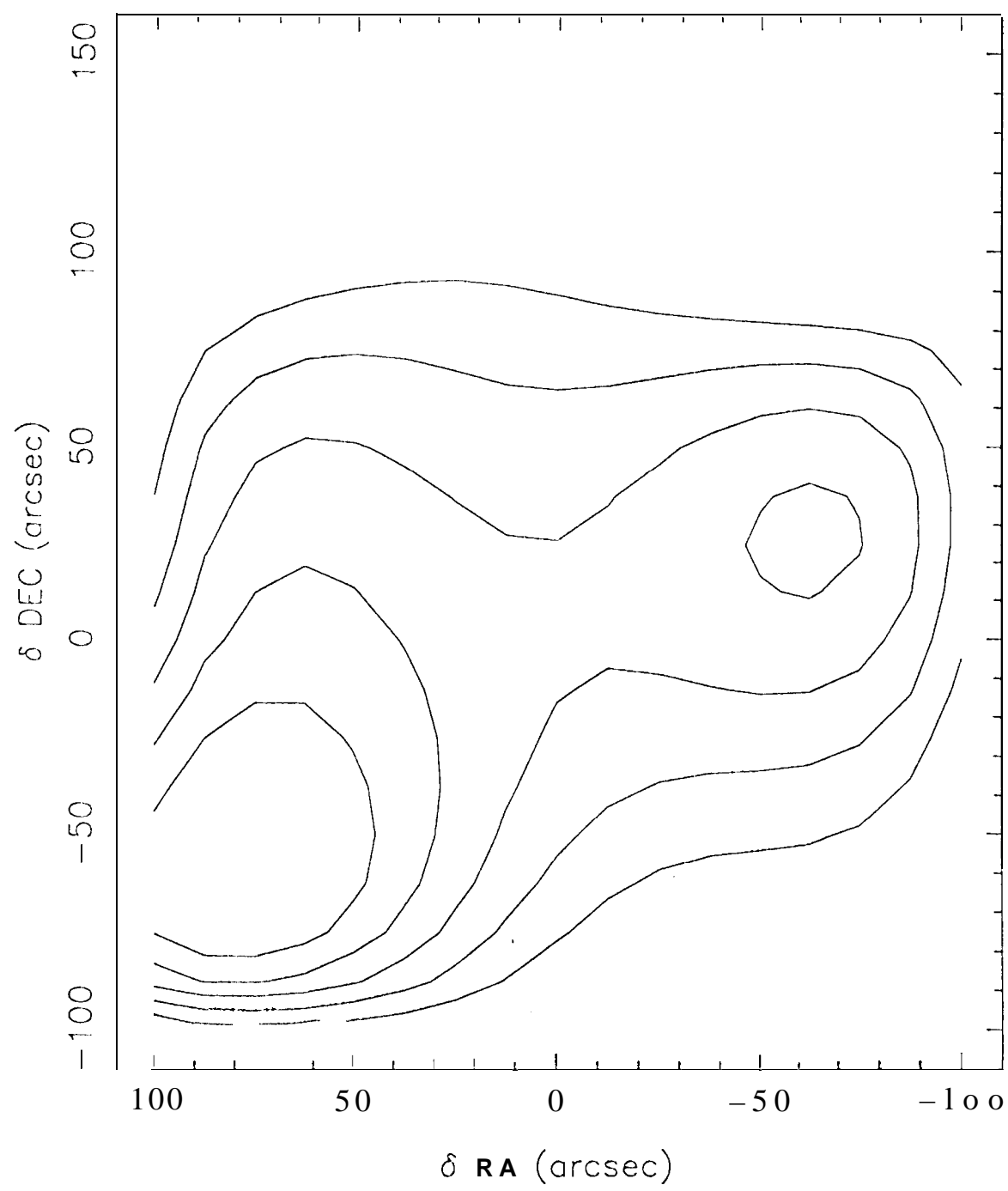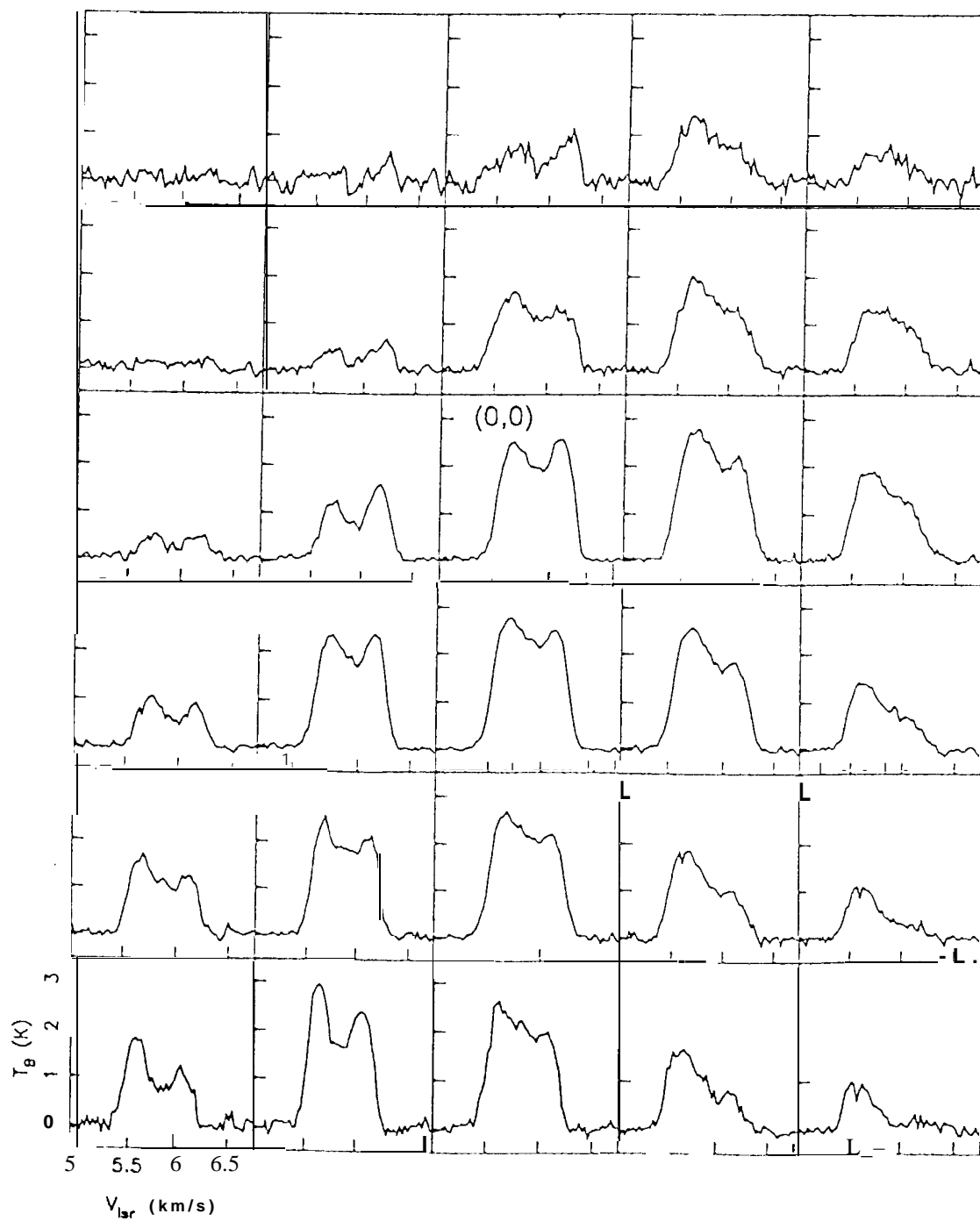
Figure 7

Figure 8

Figure 9

$T_A = 1.835 \; V = 5.684 \; \Delta v = 0.148$
$T_A = 0.954 \; V = 5.890 \; \Delta v = 0.'171$
$T_A = 1.364 \; V = 6.144 \; \Delta v = 0.132$
$\chi^2 = 0.97$

Figure 10

χ^2

Temperature (K)
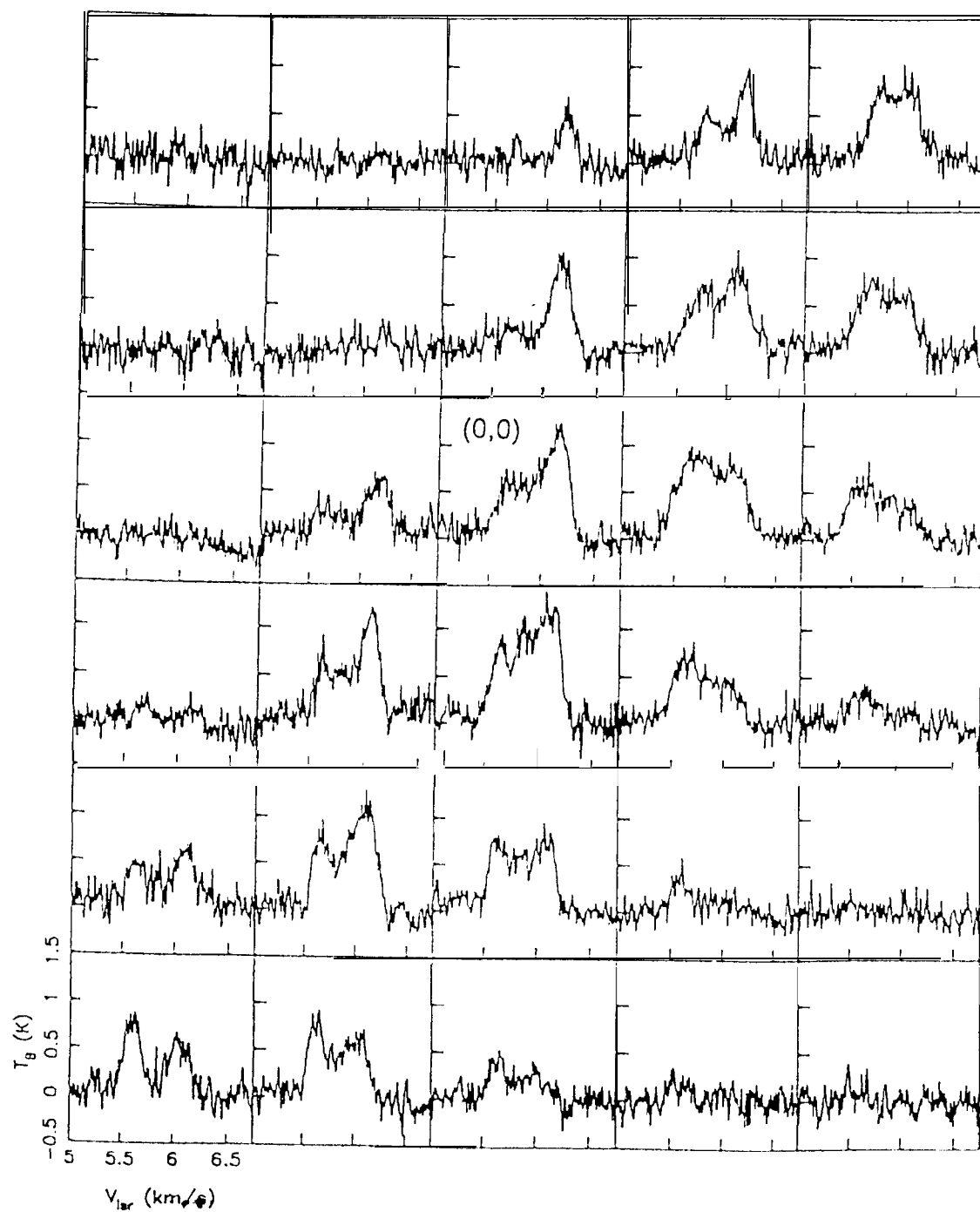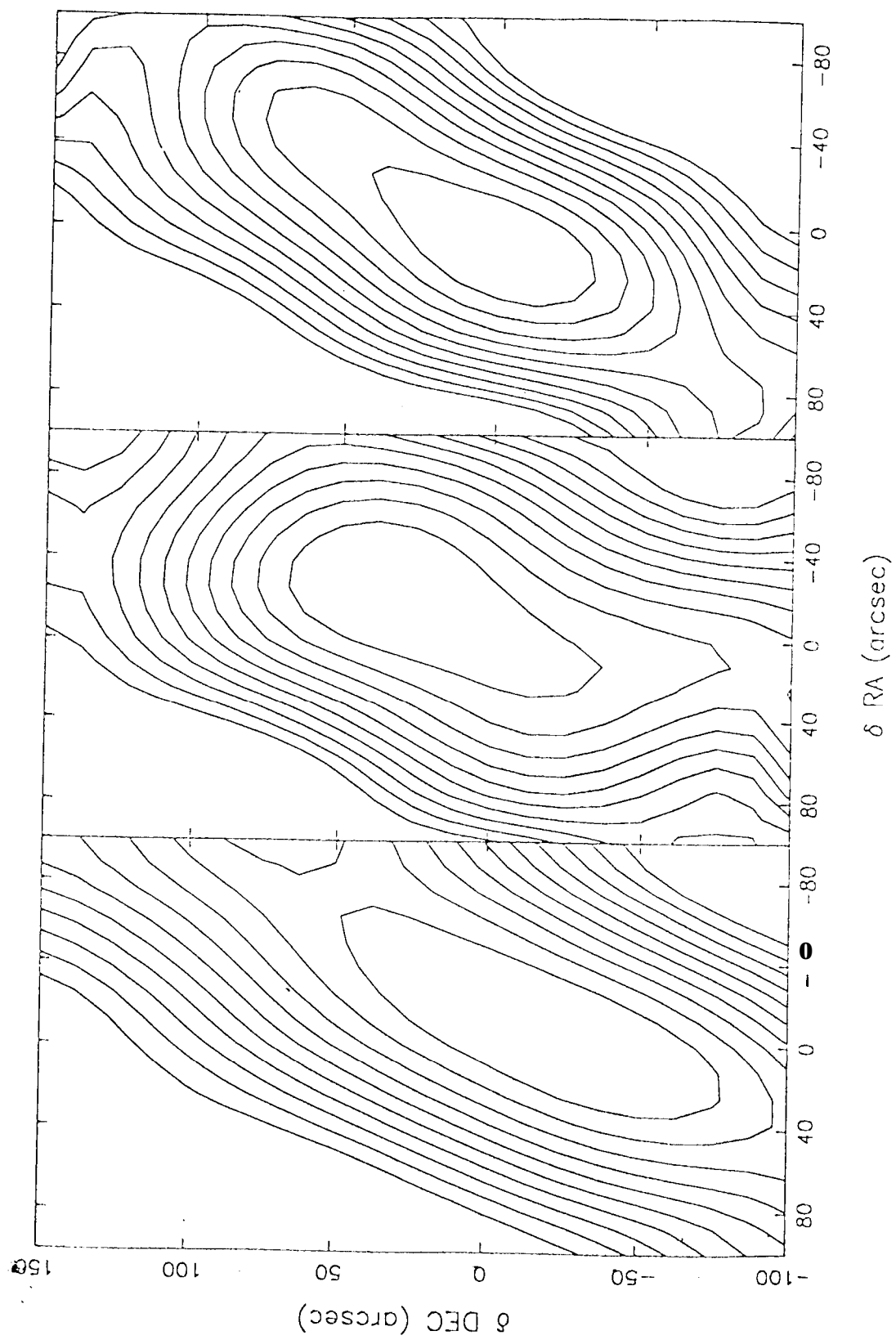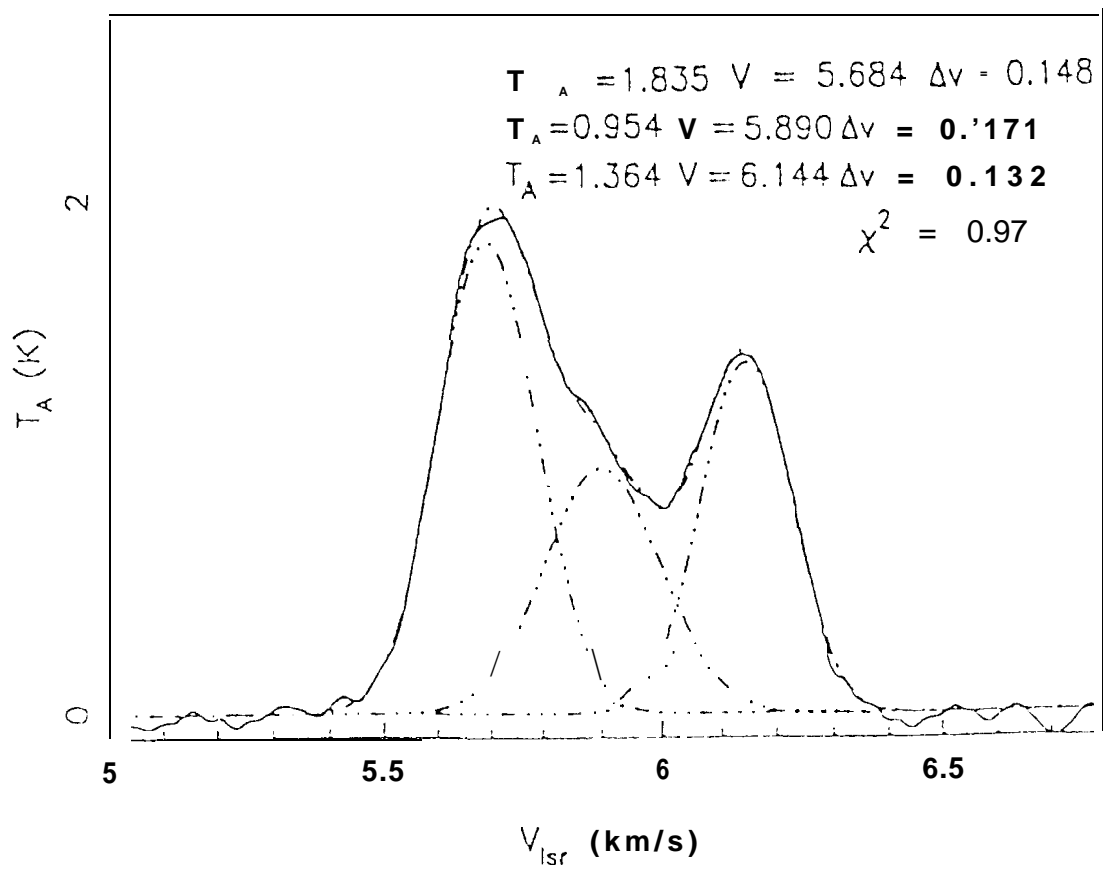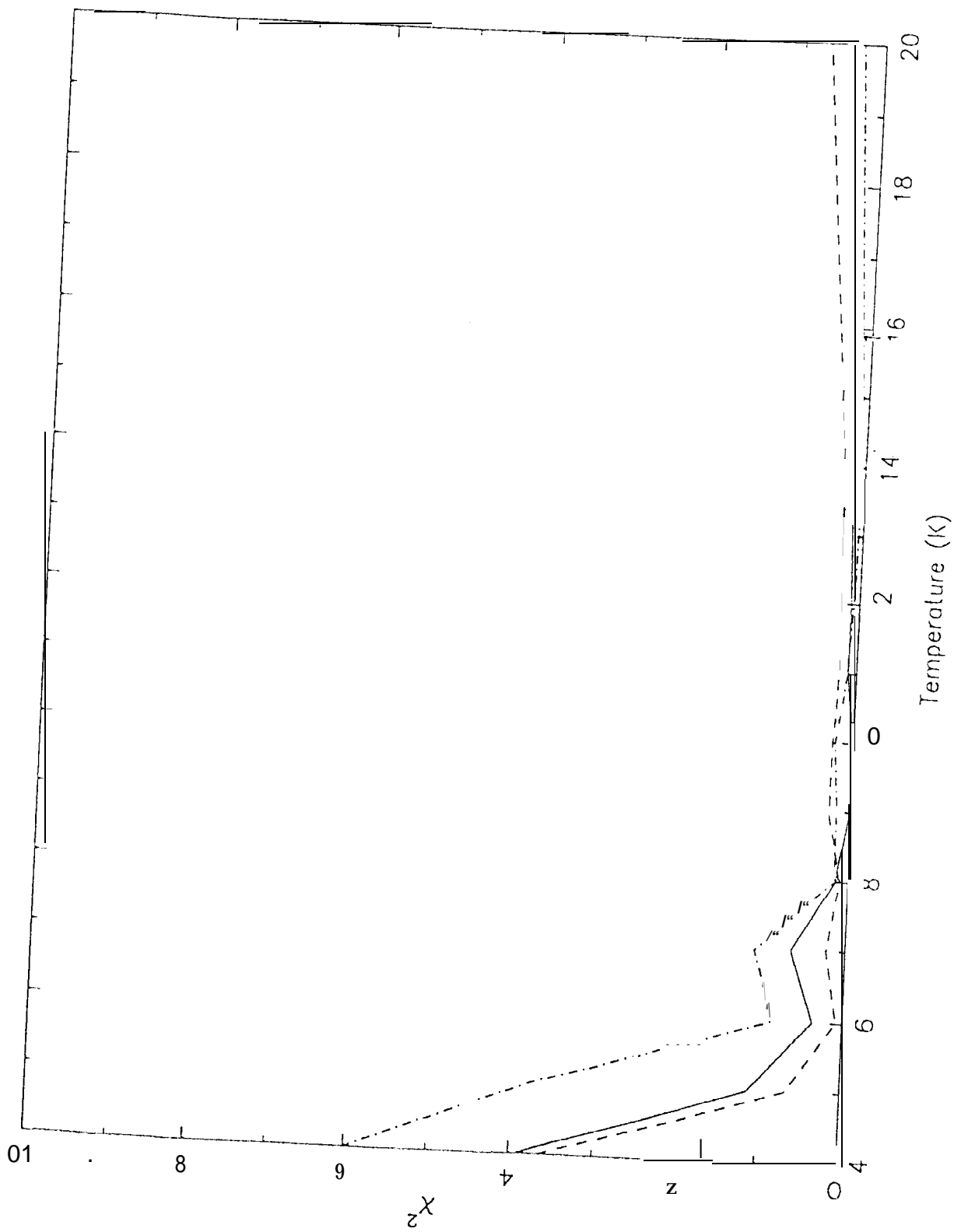
Figure 11a

Figure ‘11b

Figure 12

min. χ^2 = 0.22
χ^2 = 1.22
χ^2 = 4.22
χ^2 = 7.22
χ^2 = 15.22
χ^2 = 30.22
χ^2 = 60.22

$\log_{10} X(CCS)/(dV/dr)$ $(km^{-1}\ s\ pc)$

$\log_{10} n(H_2)\ (cm^{-3})$
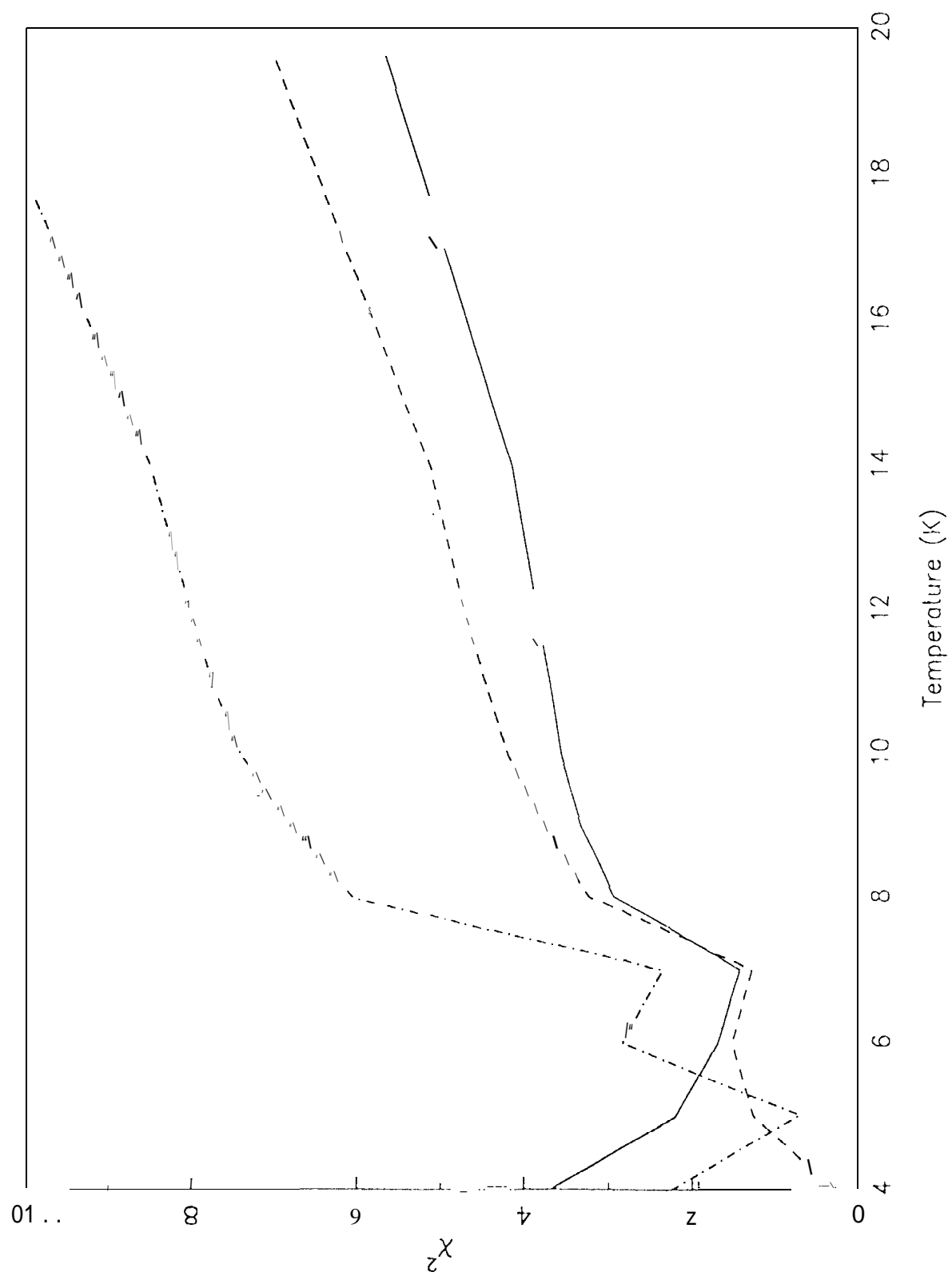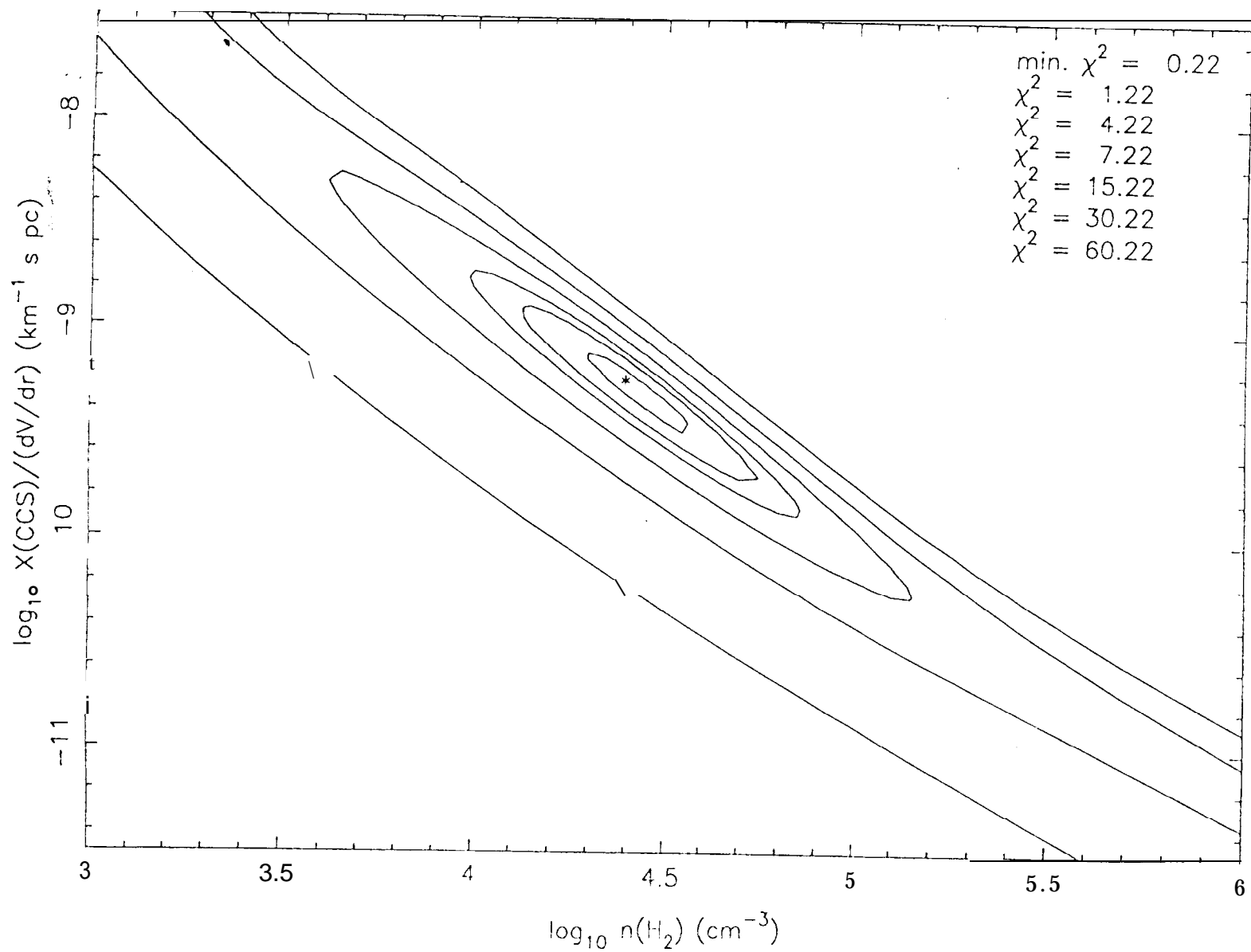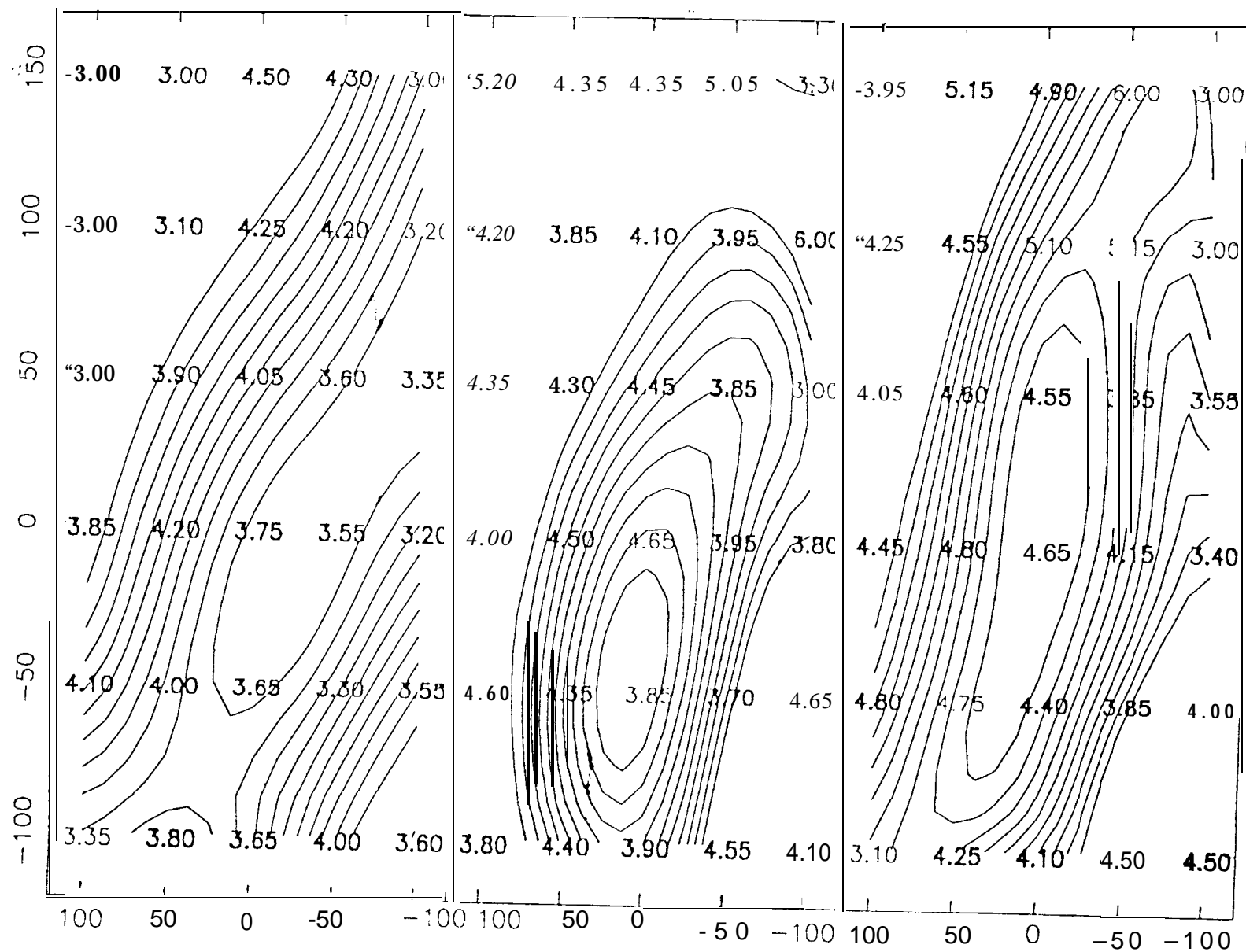
Figure 13
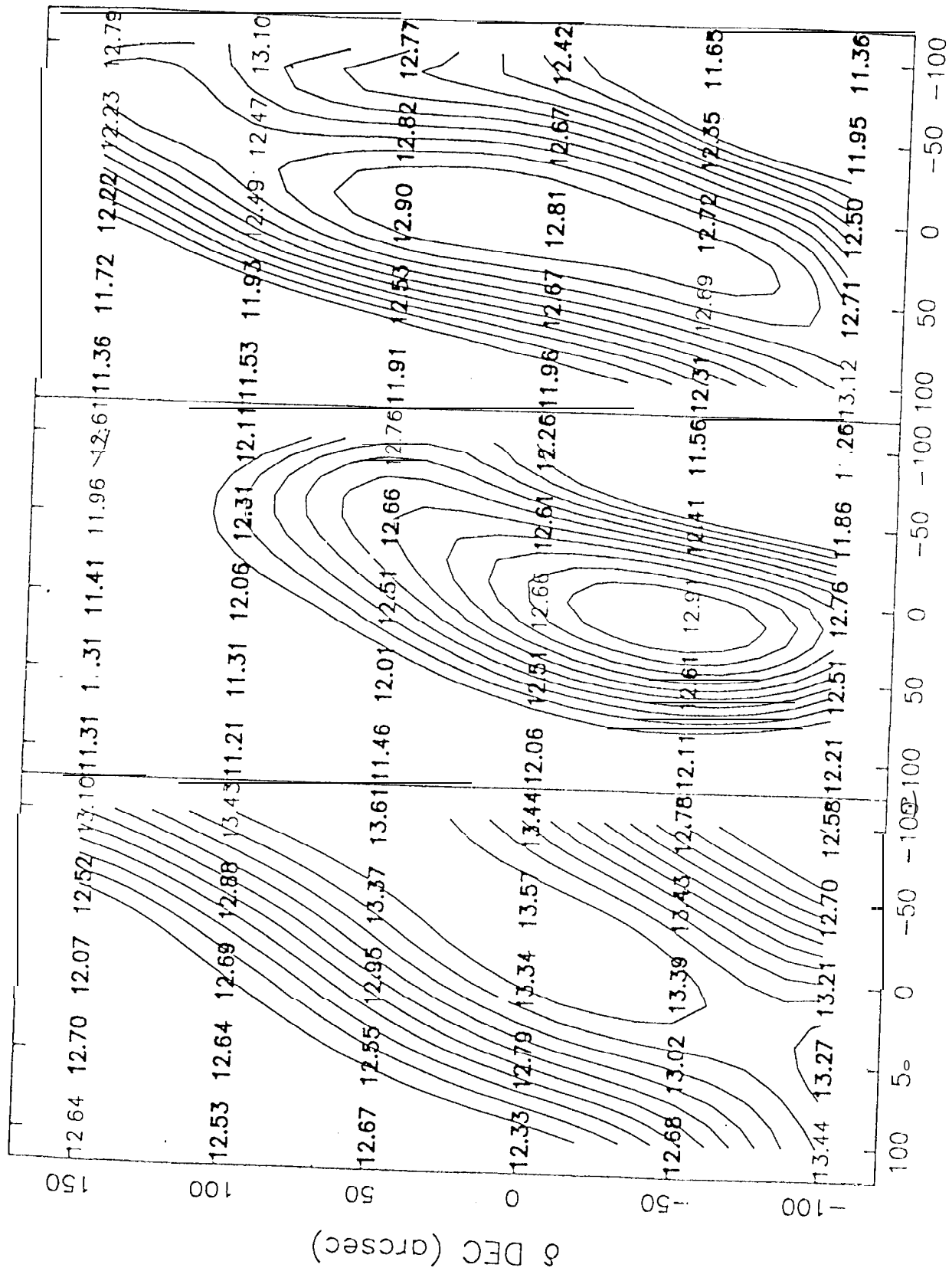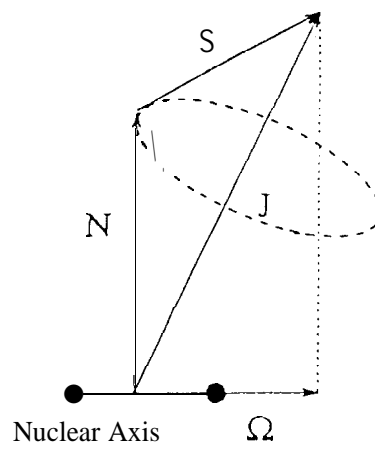
δ RA (arcsec)

δ DEC (arcsec)
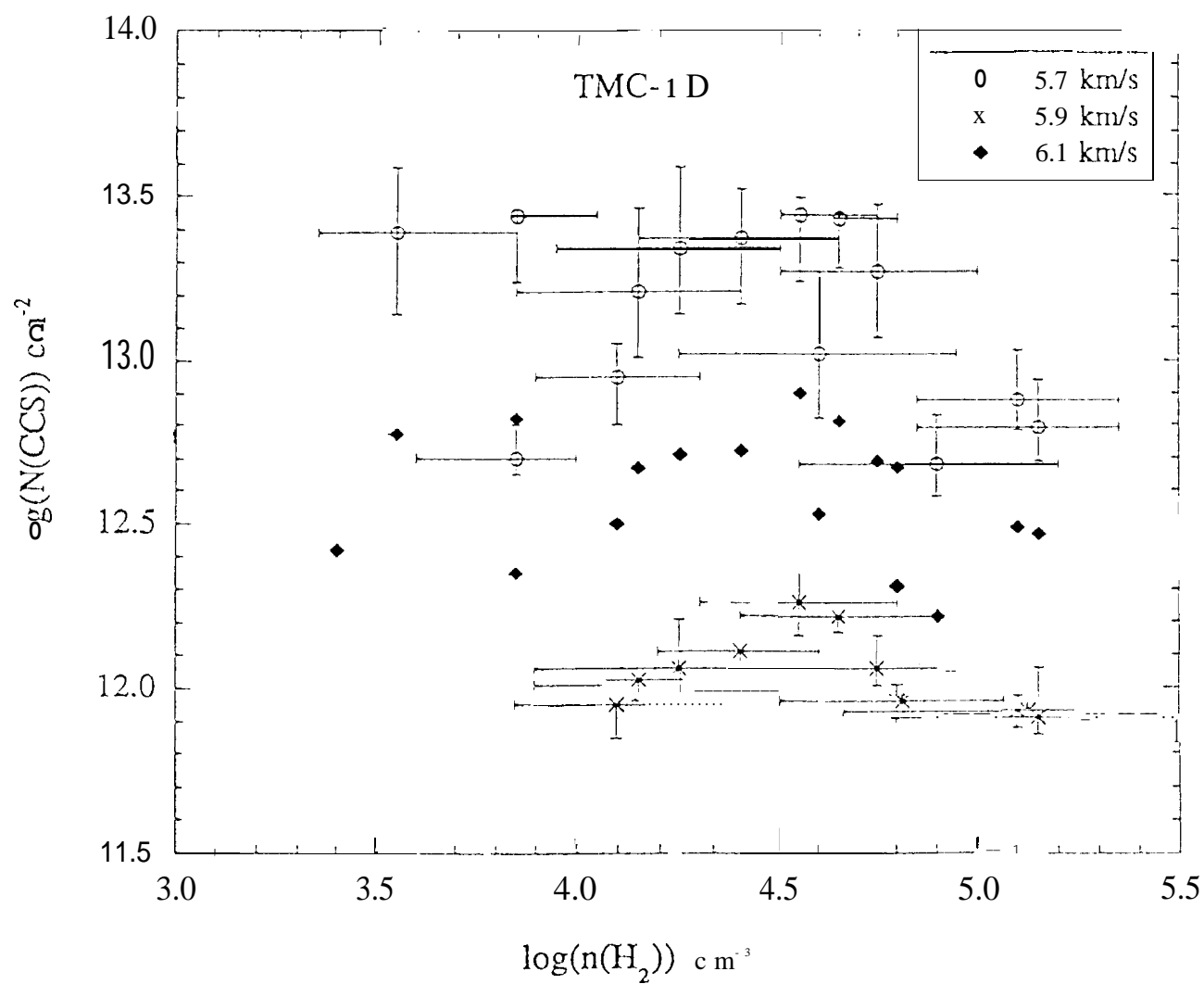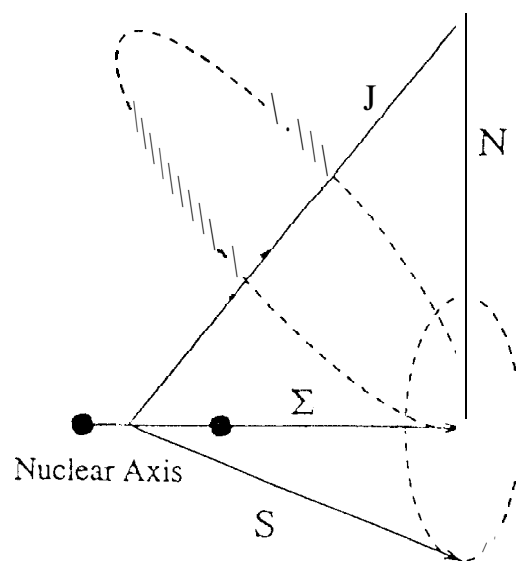
Figure 15

Figure 16

16 ◂ ◂ ▸ ▸

Figure 17

CCS Energy Levels

Figure 18